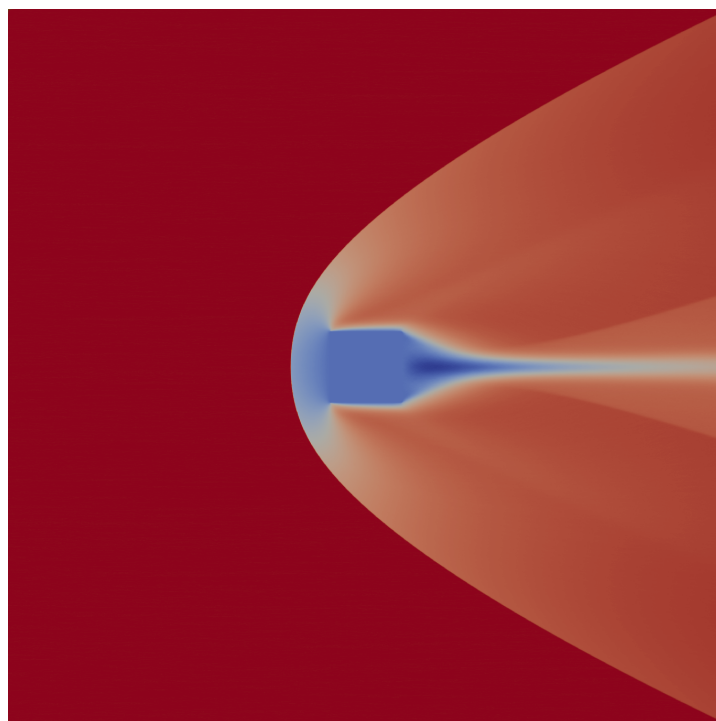

Hypersonic foldable Aeroshell for Thermal protection using ORigami (HATHOR)

Aerothermal analysis

Final Year Project



Student: Luca Mazzotta

CID: 01782839

Date: 05/06/2023

Supervisor: Dr. Paul Bruce

Second marker: Dr. Maria Ribera Vicent

Department: Department of Aeronautics

Course: H415 MEng Aeronautics
with Spacecraft Engineering

Academic year: 2022/2023

Department of Aeronautics
South Kensington Campus
Imperial College London
London SW7 2AZ
U.K.

Abstract

Given the recent increase in interest in space exploration and the relevance of rarefied hypersonics in the development of the next generation entry vehicles, a research into the effects of global and local Knudsen number on heat transfer was deemed worth to pursue. The theoretical background for rarefied flow was outlined, and relevant research in the field was examined. It was concluded that the optimal simulation method to carry out said research was Direct Simulation Monte Carlo. The method was thus explored, and four sets of simulations were designed: varying global Knudsen number, varying edge radius, varying angle of attack and constant local Knudsen number. The simulation were designed around simple geometries, such as circles and squares, in order to limit the number of variables. Convergence studies were thus carried out and the simulation results validated. From the simulations a drastic change in flow physics with rarefaction was noted, and a theoretical explanation was provided. Moreover, the dependence of the ratio between the peak and stagnation Stanton numbers on a cube with Knudsen number were investigated. No conclusive evidence was however found, and the need for further studies was pointed out.

Ringraziamenti

Ai miei genitori e ai miei nonni, a cui desidero esprimere la mia gratitudine per l'amore e l'attenzione dedicati nel trasmettermi il valore della perseveranza e dell'impegno.

Contents

List of Figures	v
List of Tables	vii
1 Introduction and motivation	1
1.1 Entry, descent and landing	1
1.2 Future of EDL	2
1.3 HATHOR	3
2 Theoretical background and literature review	5
2.1 Rarefied flow	5
2.2 Rarefied flow mathematical modelling	7
2.3 Rarefied flow simulation techniques	8
2.3.1 Correction model studies	8
2.3.2 DSMC studies	9
3 Methodology	11
3.1 Direct Simulation Monte Carlo method	11
3.1.1 Particle description	11
3.1.2 Mesh	12
3.1.3 Boundary conditions	12
3.1.4 Particle motion	12
3.1.5 Particle collision selection	13
3.1.6 Intermolecular collision mechanics and models	13
3.1.7 Particle-surface interactions	14
3.1.8 Sampling and calculation of global quantities	14
3.1.9 Iterative procedure	15
3.1.10 DSMC best practices	15
3.2 Choice of software package	15
3.3 Simulation design	16
3.3.1 Common parameters	17
3.3.2 Varying global Knudsen number	17

3.3.3	Varying edge radius	18
3.3.4	Varying angle of attack	18
3.3.5	Constant local Knudsen number	18
3.4	Convergence studies	19
3.4.1	Mesh convergence study	19
3.4.2	Number of simulated particles convergence study	22
3.4.3	Simulation convergence study	23
3.4.4	Sampling time convergence study	24
3.5	Data post processing	24
3.5.1	Equivalent square coordinate	24
3.5.2	Stanton number	25
3.5.3	Local Knudsen number	25
3.5.4	Stagnation point Stanton number	26
3.6	Validation of results	26
4	Results and discussion	28
4.1	Variation of global Knudsen number results	28
4.2	Variation of edge radius results	32
4.3	Constant local Knudsen number results	36
4.4	Variation of angle of attack results	38
4.5	Comparison of Stanton number ratio results	38
4.6	General considerations on the Direct Simulation Monte Carlo technique	39
5	Conclusion and future work	40

List of Figures

1	Sketches of HATHOR [8].	3
2	Flow regime with varying Knudsen number [1].	5
3	Schematic diagram of velocity slip (A) and temperature jump (B) [13].	6
4	Stanton number profiles along the rib section at $\alpha = 0$, $t = 5$ s. From the left: Sharp (a), Shoulder (b), Smooth (c), Sphere-cone (d) [11].	6
5	Comparisons of experimental and numerical Stanton number along the geometrical centrelines of a cube at 5 deg incidence, in a Mach 5 flow and at a range of Reynolds numbers [15].	7
6	Flowchart of Burnett and Super Burnett equations derivation [14].	9
7	Flowchart of DSMC method loop. Adapted from [35].	16
8	Heat transfer vs square equivalent coordinate for varying number of mesh elements.	20
9	Stagnation point heat transfer vs number of cells per dimension (left) and cell size (right).	21
10	Peak heat transfer vs number of cells per dimension (left) and cell size (right).	21
11	Drag coefficient vs number of cells per dimension (left) and cell size (right).	21
12	Heat transfer vs square equivalent coordinate for varying number of particles.	23
13	Velocity contours for 1 (left) and 100 (right) particles per cell.	23
14	Total number of particles vs number of time steps.	24
15	Heat transfer vs square equivalent coordinate for varying sampling time.	25
16	Best fit residuals vs number of time steps (left) and inverse of number of time steps (right).	26
17	Equivalent square coordinate illustration.	26
18	Velocity contours around a rounded square for varying Knudsen number.	29
19	Particle contours around a rounded square for varying Knudsen number.	30
20	Distribution of heat transfer along the square contour for varying values of Knudsen number	31
21	Distribution of normalised heat transfer along the square contour for varying values of Knudsen number	31
22	Distribution of modified Stanton number along the square contour for varying values of Knudsen number	31
23	Velocity contours around a circle for varying Knudsen number.	33
24	Heating (left) and stagnation Stanton number (right) distribution around a circle for varying Knudsen number.	34
25	Stanton number vs global Knudsen number for a rounded square (a) and circle (b).	34

26	Stanton number vs global Knudsen number from literature [47].	34
27	Stanton number ratio vs local Knudsen number for the varying global Knudsen number test case.	35
28	Distribution of heat transfer along the square contour for varying values edge radius. .	35
29	Distribution of Stanton number along the square contour for varying values edge radius. .	36
30	Stanton number ratio vs local Knudsen number for the varying edge radius test case. .	36
31	Distribution of heat transfer along the square contour for constant local Knudsen number case.	37
32	Distribution of Stanton number along the square contour for constant local Knudsen number case.	37
33	Stanton number ratio vs local Knudsen number for constant local Knudsen number case. .	38
34	Distribution of heat transfer along the square contour for varying values of angle of attack.	38

List of Tables

1	Varying Knudsen number simulations flow properties	18
2	Parameters of varying edge radius simulations.	19
3	Properties of constant local Knudsen number simulations.	19
4	Properties of mesh convergence study simulations.	20
5	Comparison of experimental and simulation drag coefficients for a cube and a sphere. .	27

1 Introduction and motivation

The last decade has seen a remarkable resurgence in attention towards space exploration. After several years of decay from the heights of the moon missions, the renewed interest from governmental bodies and private companies, the technological advancements in material science and reusable rockets, and the reemergence of human spaceflight have generated a positive feedback loop that has directed major investments into the sector.

Many groundbreaking endeavours have emerged: the rise of private space companies, led by industry giants such as Elon Musk's SpaceX and Jeff Bezos' Blue Origin, has democratized and made more accessible the space sector. Revolutionary new launchers, such as the fully reusable Falcon and the super heavy Starship (with the latter recently undergoing its first test flight), have axed the cost barrier for launching payload into space, opening up unprecedented opportunities for scientific research, commercial ventures, and space exploration.

Many national and international space agencies have also demonstrated a significant increase in interest. Among various mission of the European Space Agency (ESA), the following are noteworthy:

- JUICE (launched on 14 April 2023): tasked with the exploration of Jupiter's icy moons (Europa, Ganymede and Callisto), housing a magnetometer made by Imperial College.
- ExoMars (initially scheduled for the second half of 2023, but currently postponed to 2028): ESA's astrobiology mission designated to investigate signs of past life on the red planet.
- Hera (scheduled to launch in October 2024): a mission towards the Didymos binary asteroid system tasked with examining the aftermath of a the collision between the aforementioned asteroid and DART (a previous NASA mission which investigated a method of planetary defense against near-Earth objects).

On the other side of the ocean, NASA has been engaged with building and launching the Webb space telescope. Currently stationed at the sun-earth L2 Lagrange point, it is expected to make groundbreaking discoveries thanks to its infrared camera, which will allow to see objects too distant or faint to be captured by earth-stationed telescopes or the Hubble telescope.

Meanwhile, NASA's Artemis program (in collaboration with ESA and JAXA) plans to establish a long-term human presence on the moon, through the construction of a permanent outpost on the lunar surface. An extraterrestrial space station, called Gateway, will also be built. It will be placed into lunar orbit and will serve as a communication hub and temporary habitation module for astronauts in deep space missions.

The increased interest in space exploration has led to the need to efficiently launch and land greater and greater payloads has emerged. While progress on the former objective has been very good (thanks, for example, to reusable rockets such as the aforementioned Falcon and Starship, or the more conventional Space Launch System), advancements in the latter area are still lacking.

1.1 Entry, descent and landing

Getting a spacecraft to safely land onto the surface of a planet is a complex undertaking, characterised by significant challenges [1]. It is composed by three parts:

- Entry, during which the spacecraft transitions from outer space into the planet's atmosphere (and hence reduces its velocity by several orders of magnitude).
- Descent, which starts after the spacecraft reaches its terminal velocity.
- Landing, the final stage during which the spacecraft is gently brought to a standstill on the planetary surface.

Among the three, atmospheric entry is the stage which poses the most threats to the vehicle's safety. Since the interplanetary transfer velocity is usually of the order of several km/s, and the most common mechanism for achieving descent is to deploy subsonic parachutes (which require the velocity magnitude not to exceed 200 to 300 m/s), a vast amount of kinetic energy has to be dissipated.

Historically, the most common and cost-effective approach to achieve atmospheric entry has been to employ aerobraking, which consists in relying on friction with the planet atmosphere to slow the spacecraft down. This method, while being significantly less expensive than others (such as using retropropulsion), poses the challenge of having to halt heat from leaking into the very sensible payload. Minimising the heat transfer to the body is thus of the utmost importance.

Peak heat transfer rate \dot{q}_{\max} and total heat load Q are determined by Equation 1 and Equation 2 respectively

$$\dot{q}_{\max} \propto \sqrt{BC \sin(FPA)} \quad (1)$$

$$Q \propto \sqrt{\frac{BC}{\sin(FPA)}} \quad (2)$$

in which BC is the ballistic coefficient and FPA is the flight path angle. Hence, both peak heating rate and the total heating on the spacecraft are proportional to the ballistic coefficient. Thus minimising BC is essential.

The ballistic coefficient can be conceptualised as a measure of the ability of a body to counteract air resistance, and is calculated as in Equation 3, where BC is the ballistic coefficient, m is the spacecraft mass, C_D is the spacecraft coefficient of drag and A is the aeroshell incident surface area.

$$BC = \frac{m}{C_D A} \quad (3)$$

Conventionally, this has been done by increasing the vehicle frontal area. However, with the increased payloads required by future missions, this will no longer be achievable, as the aeroshell size will be limited by the launcher payload fairing diameter. New techniques have thus emerged to tackle this problem.

1.2 Future of EDL

To overcome the limit of the launcher fairing size, three new aeroshell technologies have emerged:

- Mechanically deployable aeroshells, which elude the fairing size limitation by stowing the heat shield and deploying it only after separating from the payload housing [1]. Examples where this concept has been applied include ADEPT from NASA [2] (which has already undergone extensive testing [3]) and IRENE, from the Italian Space Agency (ASI) [4].
- Inflatable aeroshells (such as the HIAD concept from NASA [5]), which employ the same concept,

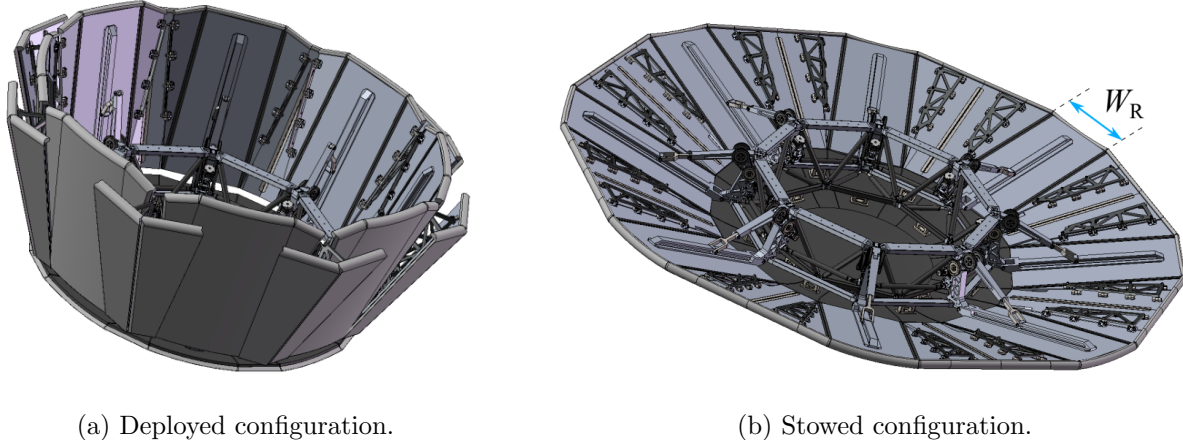
but deploy the aeroshell by inflating it rather than mechanically expanding it.

- Rigid, mid L/D aeroshells, which consist in a static fuselage-type shape which decreases BC by flying a lifting path [1, 6]

Due to their complex nature, deployable aeroshells present a fascinating set of challenges. These problems encompass structural intricacies, such as the increased failure likelihood originating from the deployment or the interlocking of the ribs for mechanically deployable ones, as well as material science complexities, such as the need of a heat shield material able to fold. Furthermore, the more sophisticated geometry makes the aerothermodynamic analysis significantly more challenging.

1.3 HATHOR

Imperial College London has also developed its own implementation of a mechanically deployable aeroshell, named HATHOR [7], which can be seen in Figure 1. It features an 2.65 m, 8 rib aluminium design with a 70 deg half cone deployed angle (which reduces to 20 deg when stowed) [7] and a 14 mm thick ablative TPS made from SLA-561 V [8]. HATHOR has undergone structural [7] and aerothermal analysis [8], and full scale mechanical testing [9].



(a) Deployed configuration.

(b) Stowed configuration.

Figure 1: Sketches of HATHOR [8].

This aerothermal analysis was conducted using both HEAT-3D [10], a reduced order model for rapid prototyping of thermal protection systems [8], and wind tunnel experiment paired with a coupled heat transfer CFD simulation [11]. In the latter, notable discrepancies emerged between the physical experiment and the simulation. These discrepancies sparked a discussion, which highlighted the possibility that they might be caused by rarefied flow, a condition known to impact aerodynamic properties.

The combination of this intriguing intuitions and their relevance in the aforementioned situation of heightened interest into space exploration served as the primary motivation behind the research presented in this thesis. The focus of this study revolves around exploring heat transfer in simple bodies under hypersonic rarefied conditions, particularly focusing on sharp corners, with the aims of investigating the evolution of Stanton number in rarefied flow and determining a correction factor to be used in codes for rapid aerothermal prototyping, such as HEAT-3D.

In section 2 the theoretical background behind rarefied flow will be investigated and relevant research about its modelling will be presented.

Section 3 will outline the general principles of operations of a Direct Simulation Monte Carlo code, which will subsequently be used to design and validate four set of simulations: varying global Knudsen number, varying edge radius, constant local Knudsen number and varying angle of attack. a full set of convergence studies will also be conducted, in order to ensure the accuracy of the simulations.

The main findings of the research will thus be outlined and discussed in section 4.

2 Theoretical background and literature review

2.1 Rarefied flow

Rarefied flow refers to a set of flow conditions where the gas is so rarefied that the continuum assumption of ordinary fluid mechanics becomes invalid [1]. Because of this, statistical mechanics has to be employed to describe it, rather than continuum mechanics.

It is possible to determine whether a flow is rarefied through the Knudsen number, a dimensionless number defined by Equation 4, where λ is the mean free path of the flow molecules and l is a characteristic length of the flow.

$$Kn = \frac{\lambda}{l} \quad (4)$$

Figure 2 shows that flows can be divided into three categories based on Knudsen number:

- For Knudsen numbers below 10^{-2} , the flow is classified as continuum. This kind of flow is characterised with a very significant number of intermolecular collision [1, 12], and is commonly observed in everyday conditions, such as the flow around the wing of an aircraft or the flow of water in a pipe. It can be mathematically modelled through the Navier-Stokes equations.
- For Knudsen numbers between 10^{-2} and 10^1 , is defined as slip. In this condition the number of collisions between molecules is low, but not negligible [12]. This leads to notable phenomena such as the boundary temperature jump, where the flow temperature at the wall differs from the surface wall temperature [13]. Moreover, a boundary slip velocity condition arises, which negates the no-slip condition observed in ordinary flows [13]. These phenomena are schematically represented in Figure 3. The modelling of this regime depends on Kn . For conditions which approach the continuum flow, this regime can be modeled by incorporating correction factors into the Navier Stokes equations [13] (in order to account for the aforementioned phenomena). Alternatively, it can be described through the Burnett and super Burnett equations [14].
- For Knudsen numbers above 10^1 , the flow is classified as free molecular flow. In this regime, intermolecular collisions are so rare that the notion of an ordered flow of molecules ceases to exist [1, 12], and is replaced by a statistical description, in the form of the Boltzmann equation.

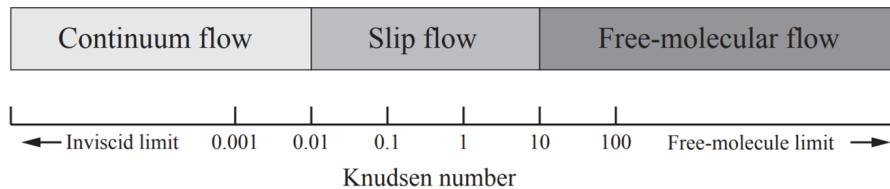


Figure 2: Flow regime with varying Knudsen number [1].

It is important to note that while a flow may be globally continuous, certain local regions may exhibit signs of rarefied flow. An illustrative example of this phenomenon is the re-entry path of the space shuttle. While at a certain altitude the global Knudsen number, calculated based on the length of the vehicle, may fall within the continuum regime, the Knudsen number associated with the flow around one of the rivets on its wing could differ significantly, potentially resulting in a different regime altogether.

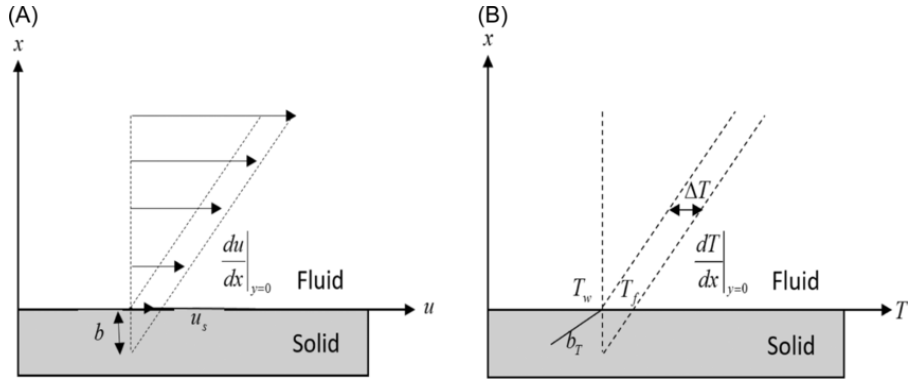


Figure 3: Schematic diagram of velocity slip (A) and temperature jump (B) [13].

Precisely this intriguing dichotomy served as the explicit catalyst for this research project: as previously mentioned, the HATHOR aeroshell was analysed through both an experiment and CHT CFD [11]. This analysis was conducted on four different geometries: sharp (shown in Figure 4a, which represents the frontal shape of HATHOR), shoulder (shown in Figure 4b, which has an open backshell to investigate the effect of the low thickness of the heatshield), smooth (shown in Figure 4c, similar to the sharp geometry but with smooth ribs to analyse the effect of ribs sharpness) and sphere cone (shown in Figure 4d, resembling a standard, non folding aeroshell).

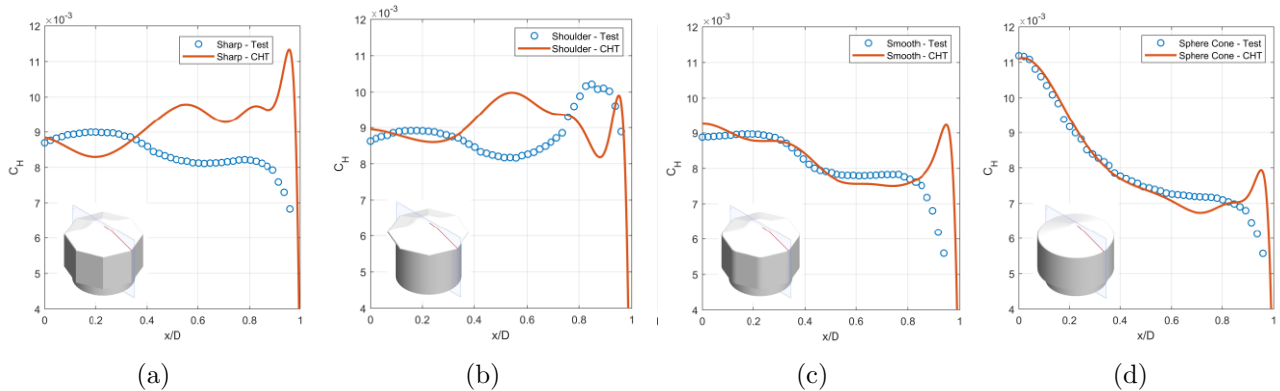


Figure 4: Stanton number profiles along the rib section at $\alpha = 0$, $t = 5$ s. From the left: Sharp (a), Shoulder (b), Smooth (c), Sphere-cone (d) [11].

From Figure 4 it is evident that significant discrepancies are present between the experimental and simulation trends. These discrepancies were the most significant in correspondence of minor geometrical features, such as the aeroshell edge and the juncture of the ribs in the sharp and shoulder models. Given the small scale of these features when compared to the geometries themselves, it was theorised that they might be inducing rarefaction effects.

Similar patterns were noted in the analysis conducted by Rees *et al.* on cubes [15]. In this paper, the hypersonic flow around cubes at incidence was analysed, both through the DLR-TAU CFD code and through a wind tunnel experiment. Figure 5 highlights the significant discontinuities observed in the modified Stanton number produced by the simulation at the cube edge (corresponding to $z/L = 0$). Again, given the small dimension of the cube edge radius, it was thought they might be caused by a local rarefaction zone.

To verify the aforementioned hypotheses, local Knudsen numbers were calculated for both of the experiments. Characteristic lengths of 7×10^{-4} m were used for the ribs in [11] and 1×10^{-4} m for

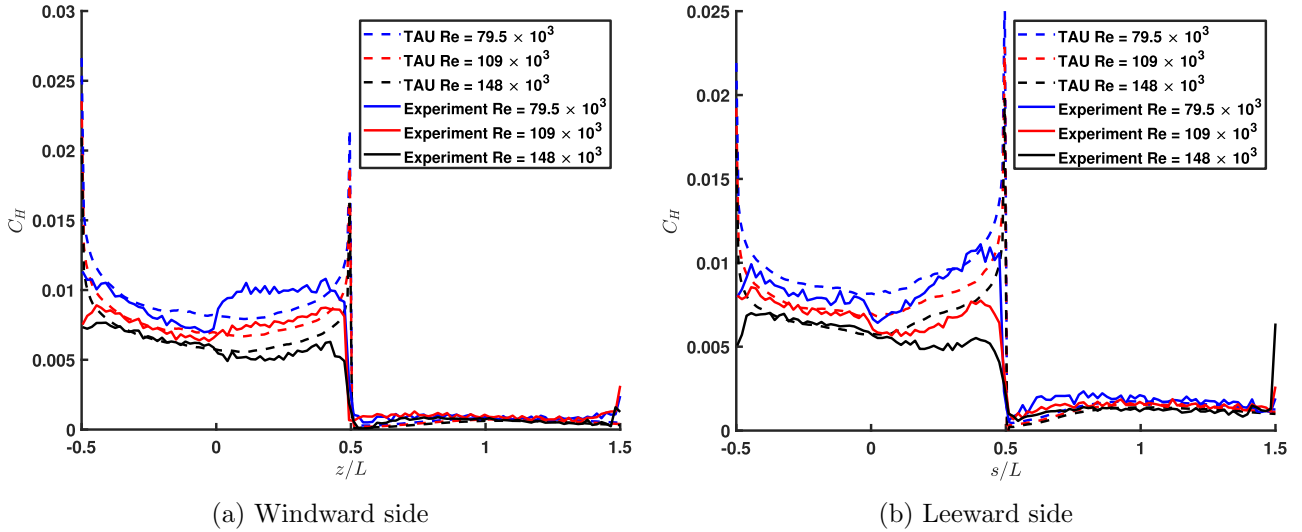


Figure 5: Comparisons of experimental and numerical Stanton number along the geometrical centre-lines of a cube at 5 deg incidence, in a Mach 5 flow and at a range of Reynolds numbers [15].

the aeroshell and cube edges (taken from the machining tolerance in [15]). It was discovered that although the global Knudsen numbers were in the order of 10^{-5} in both the papers, local Knudsen numbers increased significantly, to the order of 10^{-2} , nearing the slip regime.

It was thus considered worthwhile to conduct an in depth study of the effect of rarefaction, which is outlined in this thesis. Simple shapes were chosen for the analysis, in order to eliminate the effect that unnecessary variables, such as the half angle or the nose radius of an aeroshell, could have on the flow.

2.2 Rarefied flow mathematical modelling

As mentioned previously, Navier-Stokes equations cease to be valid in the rarefied flow regime. Different methods thus need to be employed for its analytical description.

Free molecular flow is modelled through the Boltzmann equation, presented in Equation 5. This equation, developed by Ludwig Boltzmann in 1872, describes the statistical behaviour of a thermodynamic system not in a state of equilibrium. The description that it gives is in terms of microscopic quantities, such as momentum \mathbf{p} and mass m of the particles, and is based on a particle distribution function $f(\mathbf{x}, \mathbf{c}, t)$, which expresses the probability of finding a molecule in a volume $d\mathbf{x}$ with velocity between \mathbf{c} and $\mathbf{c} + d\mathbf{c}$ [14].

$$\frac{\partial f}{\partial t} + \frac{\mathbf{p}}{m} \cdot \nabla f + \mathbf{F} \cdot \frac{\partial f}{\partial \mathbf{p}} = \left(\frac{\partial f}{\partial t} \right)_{\text{coll}} \quad (5)$$

While this description provides an accurate representation of the system, it results to be rather complex, because of its use of microscopic quantities. Therefore, a more convenient approach would be to employ a macroscopic description of the flow, in terms of common aerodynamic quantities, such as density and flow velocity.

To solve this problem, it is possible to assume small deviations from the equilibrium conditions, and apply an expansion to the Maxwell-Boltzmann particle distribution function. This expansion is

denominated the Chapman-Enskog theory [14], and can be seen in Equation 6.

$$f = f^{(0)} + f^{(1)} + f^{(2)} + \dots = \sum_{r=0}^{\infty} f^{(r)} \quad (6)$$

It is thus possible to substitute this series expansion into the Boltzmann equation, obtaining:

- For a zeroth order approximation, the Euler equations of motion (accurate to order 0 in Knudsen number)
- For a first order approximation, the Navier-Stokes equations (accurate to order 1 in Knudsen number)
- For a second order approximation, the Burnett equations (accurate to order 2 in Knudsen number and shown in Equation 7 and Equation 8)
- For a third order approximation, the Super Burnett equations (accurate to order 3 in Knudsen number)

$$\begin{aligned} P_{ij}^{(2)} = & \omega_1 \frac{\mu^2}{p} \frac{\partial u_k}{\partial x_k} S_{ij} + \omega_2 \frac{\mu^2}{p} \left\{ \frac{\partial}{\partial x_{\langle i}} \left(F_{j\rangle} - \frac{1}{\rho} \frac{\partial p}{\partial x_{j\rangle}} \right) - \frac{\partial u_k}{\partial x_{\langle i}} \frac{\partial u_{j\rangle}}{\partial x_k} - 2 \frac{\partial u_k}{\partial x_{\langle i}} S_{j\rangle k} \right\} \\ & + \omega_3 \frac{\mu^2}{\rho T} \frac{\partial^2 T}{\partial x_{\langle i} \partial x_{j\rangle}} + \omega_4 \frac{\mu^2}{p \rho T} \frac{\partial T}{\partial x_{\langle i}} \frac{\partial p}{\partial x_{j\rangle}} + \omega_5 \frac{\mu^2}{\rho T^2} \frac{\partial T}{\partial x_{\langle i}} \frac{\partial T}{\partial x_{j\rangle}} + \omega_6 \frac{\mu^2}{p} S_{k\langle i} S_{j\rangle k} \end{aligned} \quad (7)$$

$$\begin{aligned} q_i^{(2)} = & \theta_1 \frac{\mu^2}{\rho T} \frac{\partial u_k}{\partial x_k} \frac{\partial T}{\partial x_i} + \theta_2 \frac{\mu^2}{\rho T} \left\{ -\frac{2}{3} \frac{\partial}{\partial x_i} \left(T \frac{\partial u_k}{\partial x_k} \right) - 2 \frac{\partial u_k}{\partial x_i} \frac{\partial T}{\partial x_k} \right\} \\ & + \theta_3 \frac{\mu^2}{\rho p} S_{ik} \frac{\partial p}{\partial x_k} + \theta_4 \frac{\mu^2}{\rho} \frac{\partial S_{ik}}{\partial x_k} + 3\theta_5 \frac{\mu^2}{\rho T} S_{ik} \frac{\partial T}{\partial x_k} \end{aligned} \quad (8)$$

More details about the derivations can be seen in the flowchart in Figure 6 and in [14].

It has been noted by the author of this dissertation that these equations, despite providing a correct analytical description of rarefied flows, are seldom to never used in literature for carrying out actual flow simulations. This is probably due to the existence of analytically simpler methods (which will be discussed in the following section), the difficulty of correctly computing accurate boundary conditions for Burnett equations and their linear instability to short wave disturbances [16].

2.3 Rarefied flow simulation techniques

Rarefied flow simulations are mainly divided into two categories: regular CFD codes with correction factors, and Direct Simulation Monte Carlo (DSMC) solvers.

2.3.1 Correction model studies

Correction models focus on modifying regular CFD codes with thermal conduction (mostly based on the Navier-Stokes-Fourier equations) to account for velocity slip and temperature jump. They are used for very diverse conditions, from rarefied hypersonics to micro scale flows for Micro-ElectroMechanical Systems (MEMS). A sample of these studies is presented below.

De Giorgi *et al.* [17] analysed the supersonic rarefied flow onto a planar micro-nozzle through 2D and 3D CFD simulations with a Maxwellian slip condition. Le *et al.* [18] employed the same correction

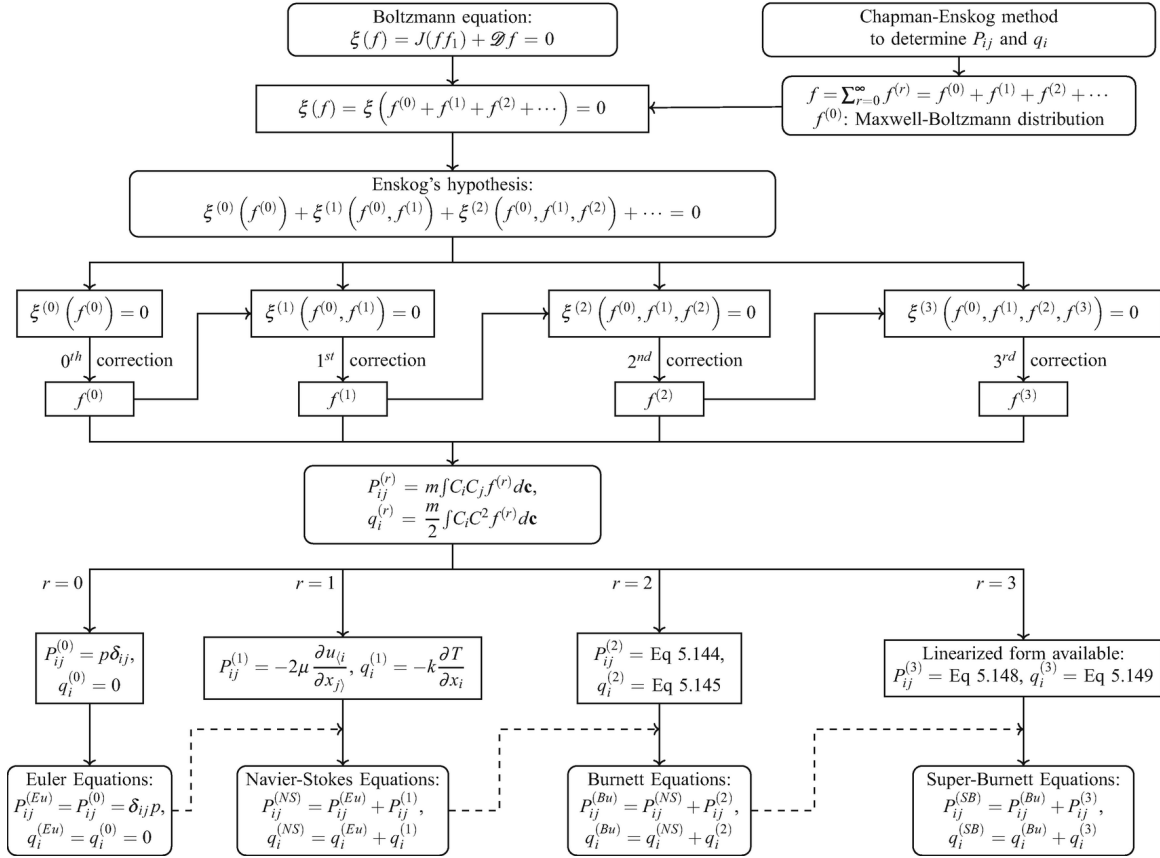


Figure 6: Flowchart of Burnett and Super Burnett equations derivation [14].

factor with second order accuracy, for the study of the flow around a 25-55 deg degree biconic and a NACA 0012 aerofoil. An improvement in results was noticed for the aerofoil, but performance remained unchanged for the biconic. Bhagat *et al.* applied a Knudsen layer correction factor to both micro scale flows (on a backwards facing step geometry) [19] and full-scale hypersonic flows (on a flat plate and a cylinder geometry) [20] noticing significant improvements in both when compared to the uncorrected CFD simulations.

Nevertheless, all of these studies reveal that the performance of correction factors falls short when compared to Direct Simulation Monte Carlo, which consistently serves as the benchmark for these techniques. Based on this evidence, it was decided to employ Direct Simulation Monte Carlo for this study.

2.3.2 DSMC studies

Quite extensive literature exists regarding DSMC studies of various geometries.

A significant number of studies are centered around cavities: Guo *et al.* [21] investigated the effect of the length to depth ratio of the cavity in the continuum, slip and transition flow regimes, characterising the flowfield inside the cavity based on these parameters. The effect of varying Knudsen number was investigated by Nabapure *et al.* [22], who observed significant variations in the Stanton number profiles at the base and on the surfaces upstream and downstream of the cavity. Jin *et al.* investigated the effect of cavity corner rounding [23], identifying a significant reduction in heat transfer to the cavity floor with the increase in radius of the aft corner.

Forward and backwards facing steps have been also analysed in depth. Nabapure *et al.* investigated the

effect of mach number and wall temperature on a backwards facing step [24], and of mach number [25], expansion ratio [26] and Knudsen number [27] on a forward facing step. The most relevant findings were the relative independence of wall temperature on the aerodynamic properties when compared to mach number, the variation in velocity profiles and heat transfer magnitudes on the forward facing step with Knudsen number, and the flow behaviour becoming independent of expansion ratio as expansion ratio itself was increased.

Blunt bodies, such as aeroshells or cylinders, are often chosen as the benchmark for validating DSMC codes or novel concepts in the statistical simulations domain. Palharini *et al.* [28] validated the dsmcFoam solver on Hypersonic rarefied non-reacting gas flows using the Mars pathfinder aeroshell geometry, noting good agreement with experimental evidence. The SPARTA DSMC code was validated on the same geometry, and on a 25-55 deg biconic [29], again finding good agreement with experimental evidence. Both of the papers noted an increase in heating at the aeroshell edge with an increase in angle of attack. Malaikannan *et al.* [30] validated an hybrid DSMC-dynamic collision limiter code on a blunt body and aerospike geometry, discovering significant reduction in computational time and negligible differences in results when compared to the standalone DSMC code. Zhonghua *et al.* [31] coupled instead a regular CFD code with DSMC, assigning domain regions to each based on the local Knudsen number. Again, good agreement was found with conventional DSMC codes.

3 Methodology

3.1 Direct Simulation Monte Carlo method

The Direct Simulation Monte Carlo method was initially introduced by Graeme A. Bird in the 1960s, and has become with time the de facto standard for rarefied flow simulations. When it was first developed, this method represented a radical departure from the traditional approaches employing a mathematical description of the flow, to such an extent that many questioned the validity of its results. It was eventually proven though, that, for time step and cell size tending to zero, the DSMC method converges to a solution of the Boltzmann equation [32].

This method models the gas as a large collection of simulated particles, each representing an even wider set of real molecules. These molecules are propagated through the simulation domain, where they collide in a stochastic manner. [33].

As the name in itself implies, this method is statistical at heart. Its results are in fact based on averaging the microscopic quantities of each of the molecules over a high number of time steps and over the grid cell size, in order to obtain global aerodynamic quantities. [32, 33]. This process will be discussed more in depth in subsubsection 3.1.8

3.1.1 Particle description

As mentioned previously, DSMC employs a particle description of the flow. The number of simulated particles is usually significantly lower than the real number of particles in the problem. This is due to the immense computational cost that simulating all of the particles in the real domain would require [34]. To provide some perspective, it is useful to consider one of the most rarefied simulations conducted as part of this thesis. In this scenario, with a Knudsen number of 10 and a density of $2 \times 10^{-7} \text{ kg/m}^3$ (a mere 0.00001% of the air density at sea level), more than 3.6×10^{18} molecules per cubic meter would have been required if a one-to-one correlation between the real and simulated molecules were to be maintained. The ratio between real and simulated molecules is expressed by f_{num} .

At the beginning of each simulation, a reference set of simulation particles is created. The microscopic properties (position and velocity) of each molecule in this set are chosen such that the bulk velocity and the global temperature of the flow correspond to the ones specified by the user, and that the number of simulated particles in the domain is equal to $\frac{n_{real}}{f_{num}}$. The individual velocity of the particles is usually selected from a Maxwell-Boltzmann distribution [34].

The simulated particles are not identical to the real particles: to correctly simulate the behaviour of the system the radius of each simulated particle must be proportional to the number of real particles that it represents, and is thus calculated such that Equation 9 (in which n is the number of particles, and σ is the particle radius) is valid. This approach also ensures the correct number of collisions in the flow [35].

$$n_{real} \sigma_{real} = n_{sim} \sigma_{sim} \quad (9)$$

No indication of how the mass of each of the simulated particles is determined has been found in literature. However, based on how the SPARTA DSMC code calculates surface quantities, it is our understanding that the mass of the simulated particles is equal to the mass of the real particles.

3.1.2 Mesh

The DSMC method discretises the domain into a collection of mesh elements. This might seem counter intuitive, as the method operates on a particle-based description of the flow, which does not require the solution of any partial differential equation.

The mesh discretisation serves two main purposes:

- It allows to reduce the computational cost: employing pure Newtonian mechanics for all the molecules within the simulation domain would be too computationally expensive [33]. Thus DSMC only computes collision of randomly selected molecules within the same cell, disregarding collisions between molecules belonging to different cells, significantly cutting the computational burden. This topic will be further discussed in more detail in subsubsection 3.1.5
- It allows the calculation of global quantities such as temperature, bulk flow velocity or density by averaging the microscopic properties of the simulated particles over the cell volume. More details about this process can be found in section subsubsection 3.1.8.

As an added benefit, discretising the domain allows parallelisation of the code by assigning chunks of cells of each processor, thus lowering the time required for the simulation.

3.1.3 Boundary conditions

One of the main advantages of the DSMC method is the ease of computing and assigning boundary conditions. Generally speaking, five boundary conditions exist [34, 36]

- Outflow boundary: particles that cross this boundary are removed from the simulation.
- Inflow boundary: this type of boundary acts as a reservoir with gas properties specified in the simulation file. Particles are emitted into the simulation based on a surface generator (where the number of particles to be injected is determined from the number flux and their velocity from a surface distribution) or a volume generator (where a layer of "ghost cells" is created and filled with particles that satisfy the reference state properties, and the ones that do not cross the boundary after the particle move are discarded) [34]. An inflow boundary also acts as an outflow boundary for particles that cross it from the simulation domain.
- Periodic boundary: the particles that cross this boundary exit the simulation and re-enter it at the opposite boundary (e.g., if the top of the simulation is a periodic boundary, particles will re-enter the simulation from the bottom) with unchanged velocity.
- Specular boundary: particles that cross this boundary reflect off of it with inverted normal velocity.
- Surface/thermal wall: particles that cross a surface are scattered based on the chosen surface-particle interaction model. More details will be given in subsubsection 3.1.7.

3.1.4 Particle motion

Particles propagate through the simulation domain based on ordinary Newtonian mechanics. Equation 10 shows the position update equation [32], where \mathbf{r} is the position vector of the particle, \mathbf{v} is the

velocity of the particle and Δt is the time step.

$$\Delta \mathbf{r} = \mathbf{v} \Delta t \quad (10)$$

3.1.5 Particle collision selection

As previously mentioned, particle collisions are handled by DSMC with a probabilistic rather than deterministic approach. While it may seem intuitive to compute the trajectories of all the particles within a cell and check for collisions for each pair, or focus on nearby particles, DSMC takes a different approach.

In DSMC collision pairs are chosen at random, without taking into consideration their position or proximity to one another. A collision probability P is then computed, and the collision is said to happen with probability P [32, 33, 34].

The sequence of steps taken is the following:

1. The number of candidate particles N_{cand} is computed based on Equation 11 [33], where N_c is the number of particles in the cell, σ is the collisional radius of the simulated molecules, $v_{r,\text{max}}$ is the maximum relative velocity and V_c is the cell volume.

$$N_{\text{cand}} = \frac{N_c^2 \pi \sigma^2 v_{r,\text{max}} f_{\text{num}} \Delta t}{2V_c} \quad (11)$$

2. A pair of potential collision partners is randomly selected among the particles in the cell, and their collisional probability P is computed. The collisional probability formula varies based on the chosen interaction model [34], but is usually proportional to both the collisional radius of the molecules and their relative velocity [32].
3. The pair is accepted as collision partners if their collision probability is higher than a random variable sampled from a uniform deviate in $(0, 1)$ [33].
4. If the pair is accepted, the velocities of the molecules are updated and the algorithm moves to the next pair. Otherwise the algorithm moves to the next pair without modifying the velocities.
5. The algorithm is repeated until the desired number of candidate particles is reached.

3.1.6 Intermolecular collision mechanics and models

When particles collide with each other, their velocities are computed based on the chosen intermolecular collision model. All of the intermolecular collision models encountered in literature are partly based on momentum conservation, as in Equation 12. The extra equations are derived based on the specific collision model

$$m_{1,i} v_{1,i} + m_{2,i} v_{2,i} = m_{1,f} v_{1,f} + m_{2,f} v_{2,f} \quad (12)$$

The three most commonly employed models are:

- Hard sphere model: this model treats molecules as impenetrable hard spheres with fixed collision diameter. Velocities are computed based on elastic collision theory [37].
- Variable hard sphere (VHS) model: this model is based on the hard sphere model, but it expands

it by considering a variable collision diameter, based on the particles relative velocity. Post collision velocities are again determined based on elastic collision theory. This method resulted in scattering which was in poor agreement with the experimental results, which led to the development of the variable soft sphere model [37].

- Variable soft sphere (VSS) model: this model introduces an extra parameter α , which governs the post collision scattering of the particles (which becomes anisotropic) [37].

Many more models exist, such as the Generalized Hard Sphere (GHS) or Lennard-Jones (L-J) models [37], but they are beyond the scope of this dissertation.

3.1.7 Particle-surface interactions

As for particle-particle interactions, many models exist for particle-surface interaction. The two most commonly used ones are:

- Specular reflection: this model reflects the particle with inverted normal velocity and unchanged parallel velocity. Since there is no change in velocity, no energy is transferred to the surface.
- Diffuse reflection: this model reflects the particles independently of their velocity before reflection. The post collision velocity is usually determined from a Maxwellian distribution based on the wall temperature [32, 36].

Many solvers allow to employ both the models at the same time through an accommodation coefficient, which determines what fraction of the collisions will be of each type.

Information about more complex models can be found in [36].

3.1.8 Sampling and calculation of global quantities

To obtain useful global quantities from the microscopic properties of the molecules, a particle sampling is executed. This consists in determining the gas macroparameters by aggregating the molecular quantities of simulated particles and averaging them over the cell volume.

Equation 13, Equation 14, and Equation 15 respectively outline the mathematical process employed to execute the sampling for density, mass-weighted average u velocity, and average kinetic energy in the SPARTA DSMC code. In the aforementioned equations f_{num} is the real to simulated particles ratio, V_c is the cell volume, N_c is the number of particles in the cell, m_i is the mass of each particle and u_i , v_i , w_i , are respectively the x , y and z components of velocity.

$$\rho = \frac{f_{num}}{V_c} \sum_{i=1}^{N_c} m_i \quad (13)$$

$$u = \frac{\sum_{i=1}^{N_c} u_i m_i}{\sum_{i=1}^{N_c} m_i} \quad (14)$$

$$KE = \frac{1}{N_c} \sum_{i=1}^{N_c} \frac{1}{2} m_i (u_i^2 + v_i^2 + w_i^2) \quad (15)$$

A similar procedure can be employed to get surface-specific values, such as the heat transfer or the force applied to a surface element.

Given the statistical noise inherent of a Monte Carlo method, the macroscopic quantities are also usually averaged over a number of time steps.

3.1.9 Iterative procedure

When a Direct Simulation Monte Carlo code is run, the following procedure, illustrated in Figure 7, is executed:

1. A random seed for the simulation is set. This set will be used to randomly generate the set of initial particles and the particles emitted by the inflow boundaries.
2. The simulation domain is created, the mesh and the reference set of initial particles are generated, and the internal geometry is loaded.
3. The number of iterations n and the initial time t are set to zero.
4. The particles are propagated through the simulation domain as described in subsubsection 3.1.4.
5. Collisions between particles and boundaries/surfaces is checked. New velocities of the particles are computed and assigned. Particles are inserted into or removed from the domain.
6. Particles are indexed, meaning their position is used to determine to which cell they belong to, to subsequently compute inter-particle collisions.
7. Inter-particle collisions are computed and new velocities assigned.
8. n is incremented by 1, t by Δt .
9. If the simulation has reached steady state, the particle sampling is executed as described in subsubsection 3.1.8, otherwise the loop continues.
10. If the final time has been reached, the results are printed and the simulation is stopped, otherwise the process goes back to step 4.

3.1.10 DSMC best practices

Literature indicates some general good practices for running DSMC algorithms. Three main parameters have to be taken into consideration for the successful execution of a simulation [38]: the mesh size, which has to be kept below one third of the mean free path [38, 39], the time step, which has to be kept below one third of the smaller between the mean collision time and the mean transition time [38], and the number of simulated particles, which has to be kept to around 20 per cell [38].

It is necessary to point out that the latter requirement has been proven to be significantly less relevant than the former two [39, 40]. However, this requirement will still be applied in the simulations, for reasons discussed in subsubsection 3.4.2.

3.2 Choice of software package

Three pieces of software were considered for running the simulations: dsmcFoam, a Direct Simulation Monte Carlo implementation part of the more general OpenFoam CFD package [41], its expansion from the rarefied hypersonics team at Strathclyde university dsmcFoam+ [42], and the SPARTA DSMC code from Sandia National Laboratories [43].

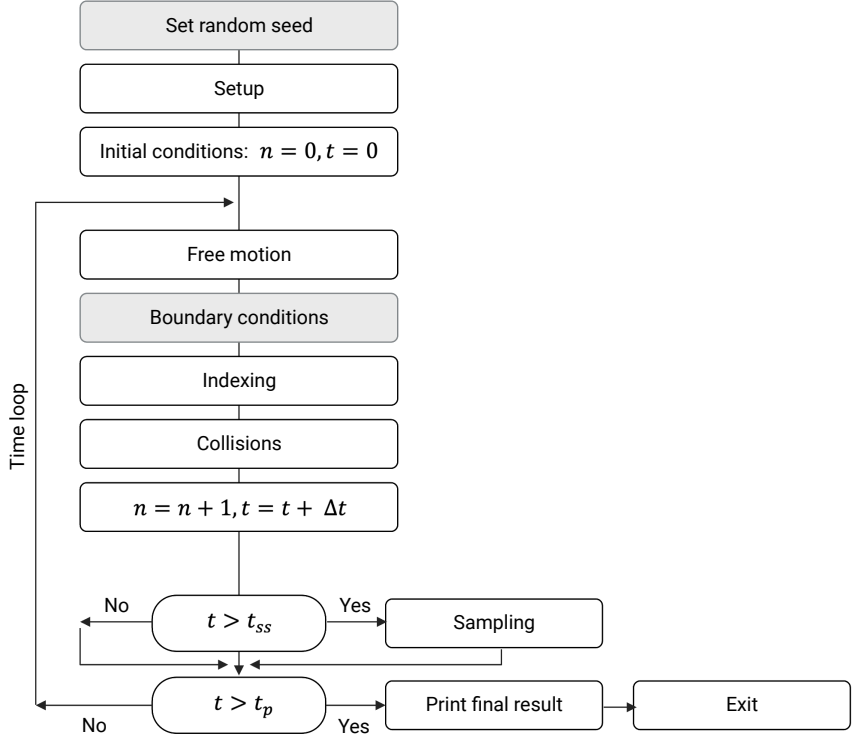


Figure 7: Flowchart of DSMC method loop. Adapted from [35].

dsmcFoam was employed for several weeks and numerous test simulations were run on it. However, it was decided to replace it, primarily due to its intricate operation and lack of readily available documentation or supportive user community. It was initially replaced it with dsmcFoam+, but some incompatibilities with the departmental HPC server prevented its use. The SPARTA DSMC package was thus chosen.

3.3 Simulation design

The simulations were designed around simple shapes, that presented the generic features and flow structure of the aeroshells in [8] while ignoring irrelevant details such as the nose radius or the cone half angle. The geometries also had to highlight the local rarefaction effects with respect to the global flow. The best geometry for this purpose was deemed to be a square with rounded corners, since it presented two edges, representative of the tip of the aeroshell, and a significant wake at the back. The rounded corner was employed to allow the control of local Knudsen number through an extra parameter. During the course of the research it was deemed useful to show how the flow features changed when taking the corner radius to extremes. The geometries of a circle (which corresponds to the radius being equal to the side of the square) and a perfect squares (radius of zero) were also simulated.

Four sets of simulations were run: constant edge radius with varying global Knudsen number, constant knudsen number with varying edge radius, constant local Knudsen number (both edge radius and global Knudsen number vary to achieve a constant Knudsen number at the corner), varying angle of attack.

3.3.1 Common parameters

Before designing the individual sets of simulations, certain parameters, applicable universally across all simulations, were determined:

- Mach number, set to 5 to replicate the one seen in [15].
- Cube size, which, as the mach number, was set to 3 cm to replicate [15].
- Simulation domain size, initially set to a square with side of 0.2 m, then increased to 0.3 m to encase the entire bow shock around the cube.
- Molecular mixture, chosen to be 22.3% of O_2 and 77.7% of N_2 by molecule count, to accurately represent the standard composition of air.
- Mixture temperature, chosen to be 273 K.
- Intermolecular collision model, chosen to be Variable Soft Sphere because of its high accuracy and relative ease of use.
- Surface collision accommodation parameter, set to 0.85 in accordance with [44]
- Surface temperature of the geometry, set to 300 K.

Some of these parameters, such as the geometry and mixture temperature, along with others that will be mentioned subsequently, were selected arbitrarily as they did not directly influence the outcome of the simulations. Their values were primarily used to generate the targeted non-dimensional numbers. For instance, to achieve a specific Reynolds number, parameters like viscosity, velocity, and size were arbitrarily fixed, and then the density was computed accordingly.

All of the simulations were run as 2D simulations, as the computational cost of DSMC would have required several months of runtime for 3D simulations.

Two more parameters were required to fully characterise the simulation: number density and real to simulated particles ratio. Their derivation will be explored in the following section.

3.3.2 Varying global Knudsen number

For the varying Knudsen number set of simulations, it was initially planned to run a set of simulations which spanned the slip flow regime (between Knudsen numbers equal to 0.01 and 10). For completeness of results, two more simulations were added towards the end of the project, at Knudsen numbers of 0.001 and 100. The chosen values can be seen in Table 1. To compute the number density for each of the test cases, the following procedure was used:

1. Determined Reynolds numbers as $\frac{M}{Kn}$.
2. Calculated flow velocity from $M = \frac{u}{a}$ with $a = \sqrt{\gamma RT}$.
3. Calculated flow viscosity from Sutherland's law.
4. Calculated density from $Re = \frac{\rho u d}{\mu}$, with d equal to the side length of the square.
5. Calculated the average molecule mass by computing the weighted average of the masses of c and N_2 , as in Equation 16.

Table 1: Varying Knudsen number simulations flow properties

Simulation	Knudsen Number	Density (kg/m ³)	Number density	Particle ratio
1	0.001	1.727×10^{-3}	3.60×10^{22}	3.24×10^{13}
2	0.01	1.727×10^{-4}	3.60×10^{21}	3.24×10^{12}
3	0.05	3.454×10^{-5}	7.20×10^{20}	6.48×10^{11}
4	0.1	1.727×10^{-5}	3.60×10^{20}	3.24×10^{11}
5	0.5	3.454×10^{-6}	7.20×10^{19}	6.48×10^{10}
6	1	1.727×10^{-6}	3.60×10^{19}	3.24×10^{10}
7	5	3.454×10^{-7}	7.20×10^{18}	6.48×10^9
8	10	1.727×10^{-7}	3.60×10^{18}	3.24×10^9
9	100	1.727×10^{-8}	3.60×10^{17}	3.24×10^8

6. Calculated the required number density by dividing the density by the average molecule mass.

$$m_{mean} = 0.223 m_{O_2} + 0.777 m_{N_2} \quad (16)$$

Having determined the number density, the ratio between real and simulated particles had to be computed. To do this, the number of real particles in the simulation domain was calculated by multiplying the density ratio by the domain volume. This value was then divided by the total number of simulated particles in the domain (computed as the product between number of cells and simulated particles per cell). The results of this calculation are shown in Table 1. The process through which the optimal number of molecules per cell and the number of cells was determined will be discussed in a following section.

The varying Kn simulations were run for both the circle and rounded square geometries. The square edge radius was set to 1×10^{-4} m. This value was chosen in accordance with the cube corner radius seen in [15].

3.3.3 Varying edge radius

The varying edge radius set of simulations was run to accomplish two objectives: illustrate the variation in flow structure as the edge radius increased from zero (representing a perfect square) to the length of the square side (forming a circle), and investigate the effect of corner radius in the change in Stanton number at the square edge. The full details of the simulations can be seen in Table 2.

3.3.4 Varying angle of attack

The varying angle of attack simulations were conducted to investigate the variation in heat transfer at the front and back of the cube with angle of attack, as this was investigated quite extensively in literature [28, 29]. The simulations were run at ± 5 , ± 10 , ± 30 and 45 deg with Knudsen number of 0.01.

3.3.5 Constant local Knudsen number

The constant local Knudsen number simulations were run while attempting to keep the local Knudsen number at the corner of the cube constant. To achieve this, a base Kn and edge radius were set for the first simulation. For subsequent simulations, the Knudsen number was multiplied by a specific factor, while the edge radius was divided by the same factor. This was done under the assumption

Table 2: Parameters of varying edge radius simulations.

Simulation	Knudsen Number	Edge radius (m)
1	0.01	0
2	0.01	2×10^{-6}
3	0.01	5×10^{-6}
4	0.01	1×10^{-5}
5	0.01	2×10^{-5}
6	0.01	5×10^{-5}
7	0.01	1×10^{-4}
8	0.01	2×10^{-4}
9	0.01	5×10^{-4}
10	0.01	1×10^{-3}
11	0.01	2×10^{-3}
12	0.01	5×10^{-3}
13	0.01	1.5×10^{-2}

Table 3: Properties of constant local Knudsen number simulations.

Simulation	Knudsen Number	Edge radius (m)
1	0.01	1×10^{-3}
2	0.05	2×10^{-4}
3	0.1	1×10^{-4}
4	0.5	2×10^{-5}
5	1	1×10^{-5}
6	5	2×10^{-6}
7	10	1×10^{-6}

that the local mean free path number would be directly proportional to the local one. The full set of parameters is shown in Table 3

3.4 Convergence studies

Having designed the simulations, a set of convergence studies was run to investigate the effect of cell size, number of simulated particles and sampling time, and to determine the necessary time for the simulation itself to converge.

3.4.1 Mesh convergence study

To determine the optimal mesh size, a set of 8 simulations was run at a Knudsen number of 0.01. All of the simulations were run with a rounded cube with edge radius of 1×10^{-4} m. In the first seven simulations, the number of mesh elements was manually increased from 100 to 3000 per domain dimension. The last simulation was run with a dynamically refining mesh, which started from 1000 mesh elements per dimension and dynamically split the cells containing more than 80 particles into four. The simulations were run for a total time of 6×10^{-4} s and the data was sampled for the last 1×10^{-4} s of the simulation. The time steps were varied in order to maintain them below a third of the mean cell transition time. The full set of simulation parameters is shown in Table 4, together with the runtime of each of the simulations.

Figure 8 shows the distribution of heat transfer rate around the square (more information about the

Table 4: Properties of mesh convergence study simulations.

Simulation	Number of cells per dimension	Cell size (m)	Time step (s)	Runtime (s)
1	100	3×10^{-3}	6×10^{-7}	21
2	300	1×10^{-3}	2×10^{-7}	1312
3	600	5×10^{-4}	1×10^{-7}	1679
4	1000	3×10^{-4}	6×10^{-8}	4621
5	1500	2×10^{-4}	4×10^{-8}	34464
6	2000	1.5×10^{-4}	3×10^{-8}	75095
7	3000	1×10^{-4}	2×10^{-8}	170914
Dynamic	4825	Not applicable	6×10^{-8}	18997

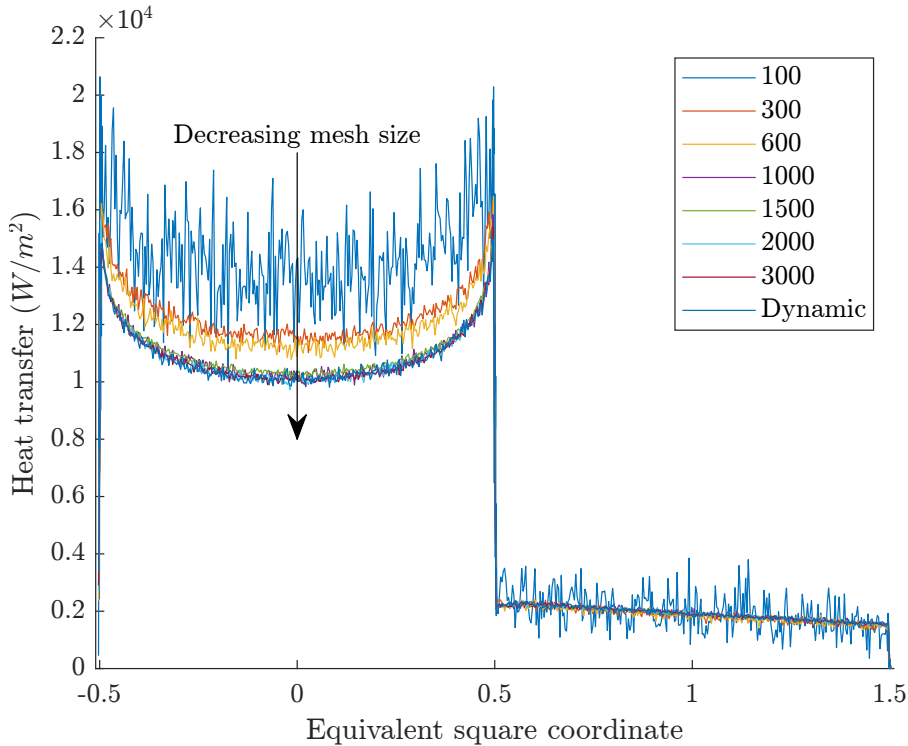


Figure 8: Heat transfer vs square equivalent coordinate for varying number of mesh elements.

x coordinate can be found in subsection 3.5) for different mesh sizes. It is possible to note that as the number of elements increases, the stagnation point heat transfer rate converges to a value of about $1 \times 10^4 \text{ W/m}^2$.

Figure 9, Figure 10 and Figure 11 respectively show how the stagnation point heat transfer, the peak heat transfer and the drag coefficient vary as the mesh resolution is increased. In these plots the dynamic mesh simulation was represented through a mesh size of 4825 elements, obtained by taking the square root of the total number of mesh elements at the end of the simulation.

As it is possible to see from these graphs, stagnation point heating and drag coefficient showed a lower sensibility to mesh size than peak heating, only showing respectively 1.5% and 0.2% of difference between the value obtained with 1000 elements and 3000 elements. Peak heating showed a slower convergence trend, only achieving full convergence past 2000 mesh elements.

Overall, all of the parameters analysed were deemed to have converged past 2000 cells per dimension. This mesh was thus validated against the best practices discussed in subsubsection 3.1.10.

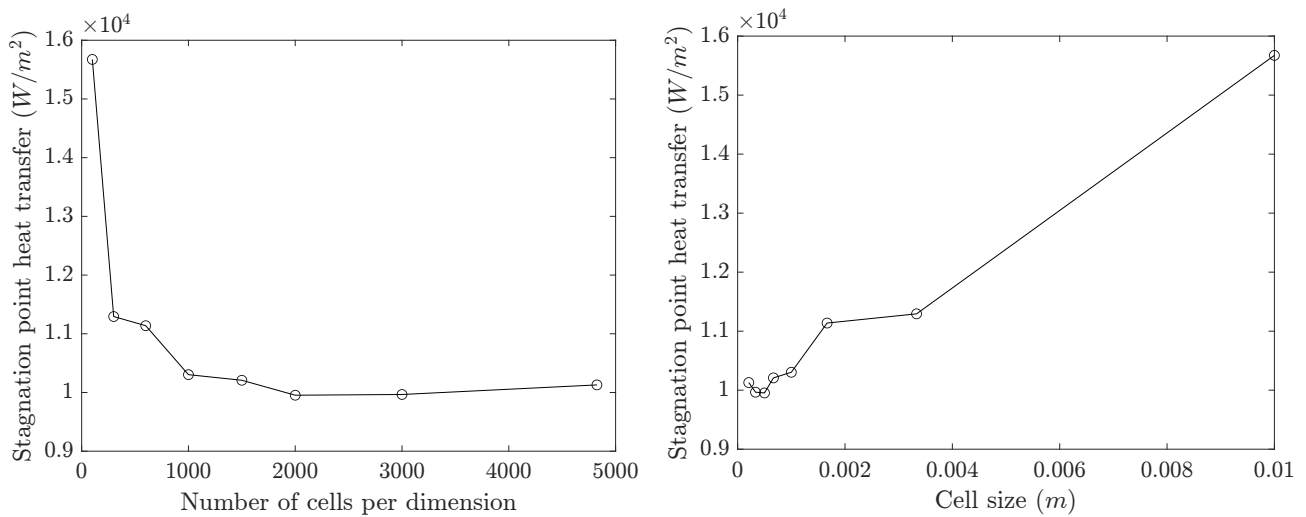


Figure 9: Stagnation point heat transfer vs number of cells per dimension (left) and cell size (right).

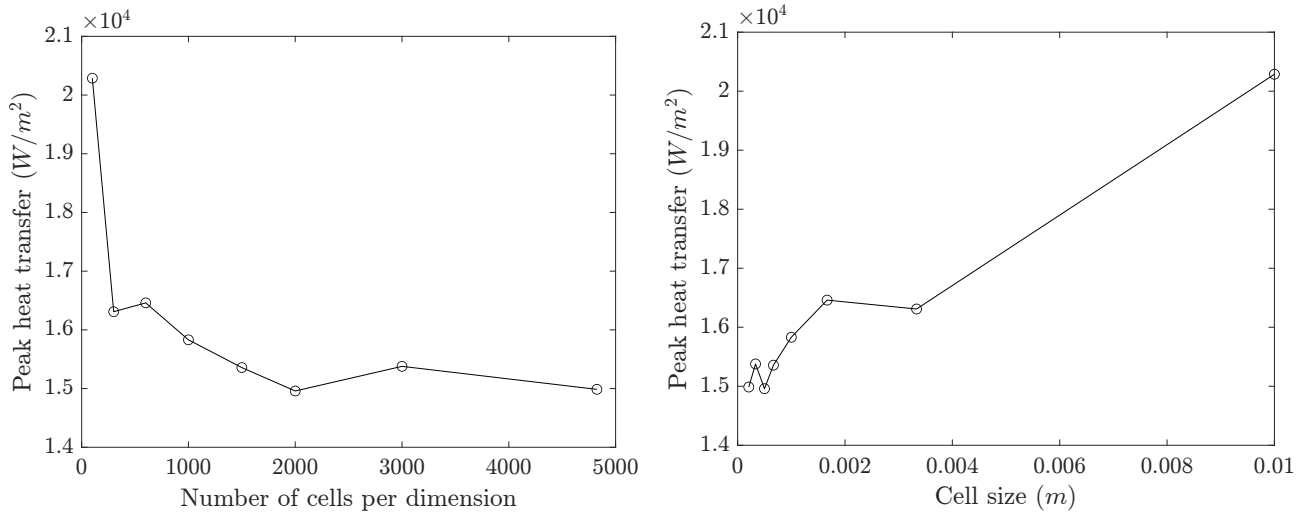


Figure 10: Peak heat transfer vs number of cells per dimension (left) and cell size (right).

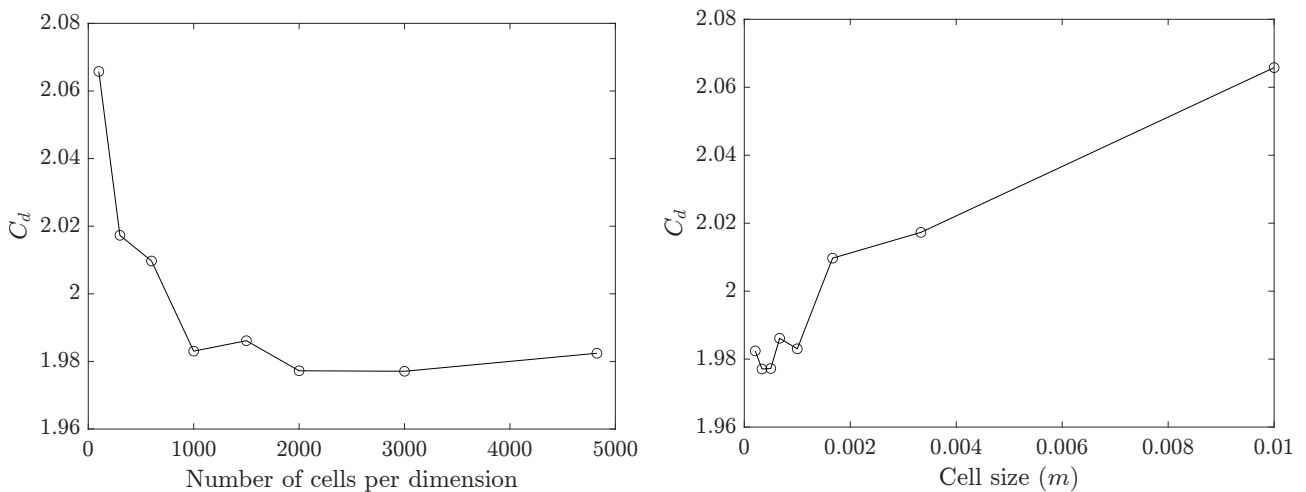


Figure 11: Drag coefficient vs number of cells per dimension (left) and cell size (right).

To do so, the mean free path was calculated to be equal to 3.9×10^{-4} m using Equation 17, with the number density n of the lowest Knudsen number simulation planned at the time (equal to 0.01), along with the weighted average of the molecular diameters of O_2 and N_2 . This value was then divided by three and juxtaposed to the cell size of the mesh. Although not smaller, the cell size was merely 15% bigger than the required size.

$$\lambda = \frac{1}{\sqrt{2}\pi d^2 n} \quad (17)$$

The mean collision time was obtained by dividing the mean free path by the mean molecular velocity, calculated through Equation 18. This was then divided by three, resulting in a value of 2.6×10^{-7} s, significantly larger than the time step for the mesh size analysed.

$$v = \sqrt{\frac{3 k_b T}{m}} \quad (18)$$

Given the only marginal discrepancy between the actual and recommended cell sizes, and the good results of the mesh convergence, this mesh size was deemed to be sufficient and selected for all of the subsequent simulations.

It is necessary to point out that since the mesh convergence was conducted before the decision of including a simulation at a Knudsen number of 0.001, the grid might not be fully converged for that case. This will be discussed in subsection 4.1.

3.4.2 Number of simulated particles convergence study

To determine the appropriate number of simulated particles, a set of 7 simulations was run at a Knudsen number of 0.01 and mesh size of 300 elements per dimension, with increasing number of particles from 1 to 100 per cell. The reduced mesh size was chosen due to the prohibitive computational cost that running the previously selected mesh would have required.

Figure 12 shows that the effect of moving from 1 to 100 particles per cell was only a reduction in the statistical noise, due to the higher number of lighter molecules hitting the surface. This was also confirmed when looking at the velocity contour plots, shown in Figure 13 for the 1 and 100 particles per cell cases.

Given the results of this analysis and what was found in literature [39, 40], the particle number was set to 25, as it was thought to be a good balance between computational cost and statistical noise.

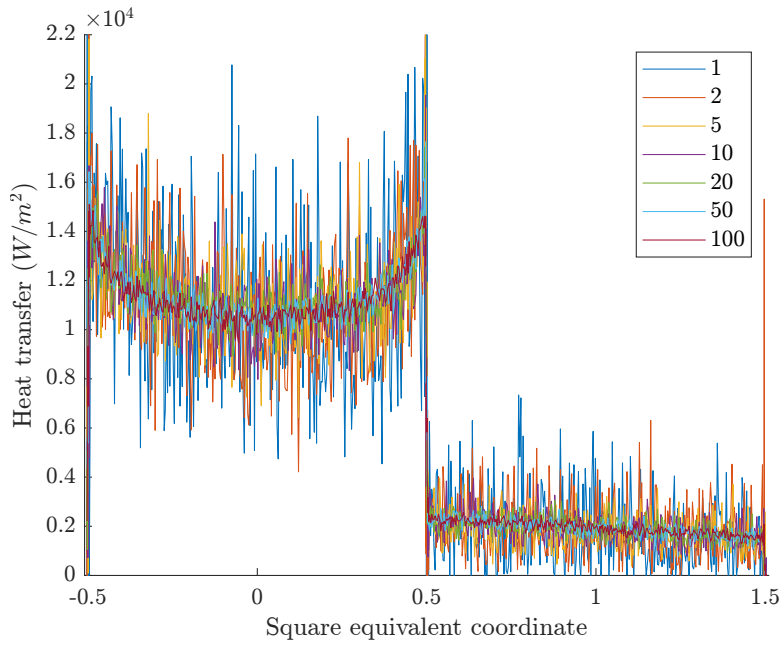


Figure 12: Heat transfer vs square equivalent coordinate for varying number of particles.

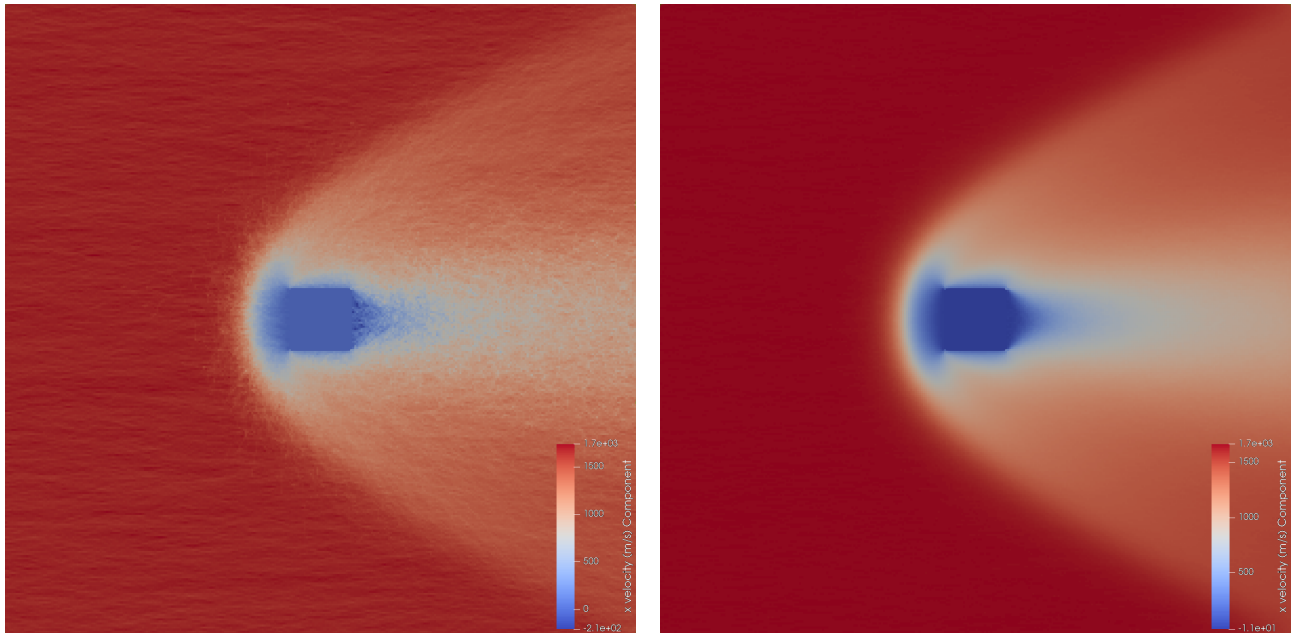


Figure 13: Velocity contours for 1 (left) and 100 (right) particles per cell.

3.4.3 Simulation convergence study

Having selected the mesh size and the number of particles, the first simulations were run. To determine at what point they reached steady state, the number of simulated particles present at a given point in the simulation was adopted as a criterion. As it is possible to see from Figure 14, the number of particles started plateauing after around 10000 time steps, and could be considered converged after 20000 time steps, corresponding to 4×10^{-4} s. This was thus chosen as the point of convergence of the simulations.

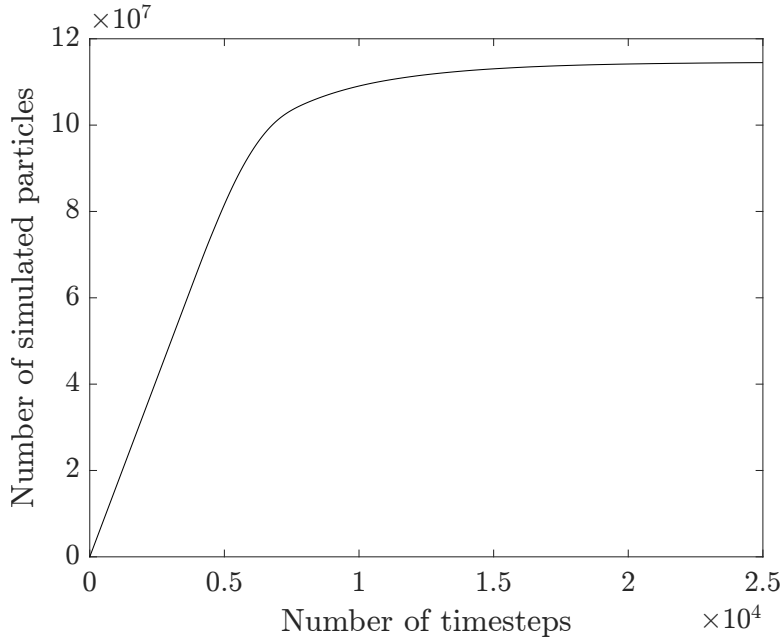


Figure 14: Total number of particles vs number of time steps.

3.4.4 Sampling time convergence study

In order to identify optimal sampling time for the macroscopic quantities, the simulation with a Knudsen number of 0.01 from the varying Knudsen number set was run for 30,000 steps. Data was sampled for the final 10,000, 5,000, 1,000, 500, and 100 time steps. The results are shown in Figure 15. To quantify the point of diminishing returns, a line of best fit was drawn through the relatively flat section between $x = 0.5$ and $x = 1.5$. The residuals of this best fine were thus computed, and plotted against the number of time steps. As visible from Figure 16, past the 5000 sampling time steps, the residuals stopped decreasing. This was thus chosen as the sampling time for all of the subsequent simulations.

3.5 Data post processing

3.5.1 Equivalent square coordinate

Having run the simulation, the heat transfer rate values obtained had to be plotted against a coordinate system suitable for all of the various geometries. An equivalent square coordinate was thus devised, which can be computed through the following procedure:

1. Inscribe the geometry in a perfect square
2. Trace a line from the centre of the perfect square to the chosen point on the geometry and extend it until it intercepts the perfect square.
3. Measure the distance from the midpoint of the left face of the perfect square to the intercepted point, tracing along the side of the perfect square.
4. Divide the measured distance by the side length of the perfect square to normalise it.

An illustration of the procedure is shown in Figure 17. N.B. The stagnation point of the body is located at 0.

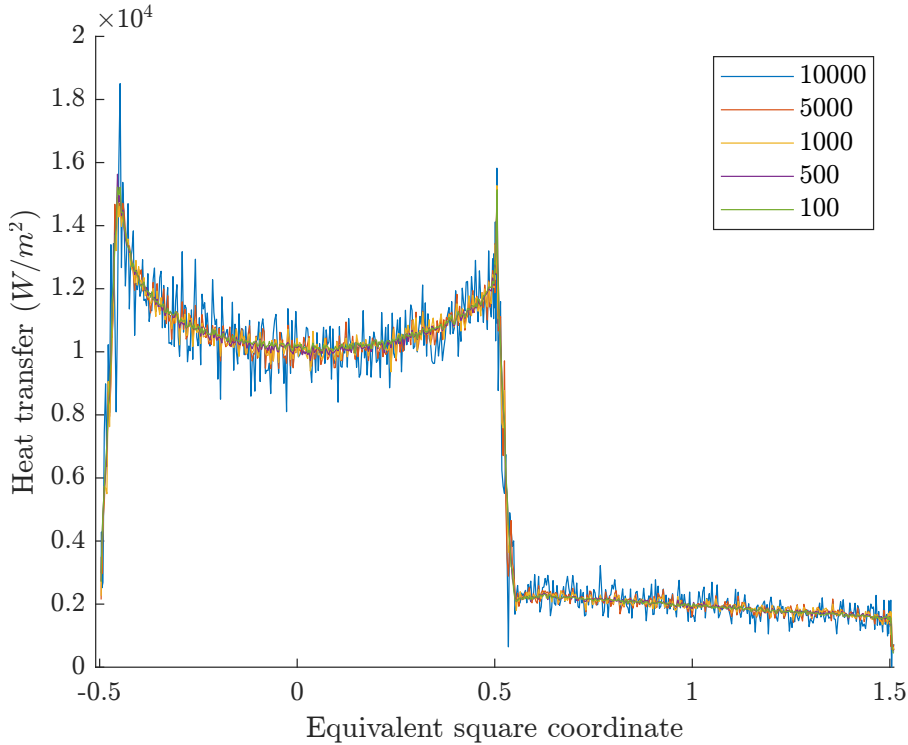


Figure 15: Heat transfer vs square equivalent coordinate for varying sampling time.

3.5.2 Stanton number

The modified Stanton number C_H was computed from the heat transfer values through Equation 19 [11, 15], where q_w is the convective heat transfer at the wall, ρ_∞ and u_∞ are density and velocity in the freestream, H_0 is the total enthalpy and h_w is the static enthalpy at the wall.

$$C_H = \frac{q_w}{\rho_\infty u_\infty (H_0 - h_w)} \quad (19)$$

3.5.3 Local Knudsen number

The local Knudsen number at the square's corner was determined as the ratio between the corner radius and the local mean free path of the flow. To do so, the mean free path was calculated through Equation 20, in which D_{ref} denotes the reference diameter of the real particles, T_{ref} represents the reference temperature, ω is the viscosity temperature-dependence for the species, and T and n are respectively the temperature and number density values. [36].

$$\lambda = \left\{ \sqrt{2} \pi D_{ref}^2 n (T_{ref} / T)^{\omega-1/2} \right\}^{-1} \quad (20)$$

It should be noted that this equation is designed for a single species flow, and not the bi-species one implemented in the experiments. Hence, the values used for reference diameter, temperature and viscosity-temperature dependence were determined by computing the weighted average of the values for O_2 and N_2 . The individual values for the two elements were also examined, showing a discrepancy in mean free path values of about 30% between the two. Although this divergence might seem substantial, given the order of magnitude differences in Knudsen number it was not deemed significant enough to warrant concern. The number density and temperature values were instead obtained from SPARTA, by sampling the values at the mesh element closest to the corner.

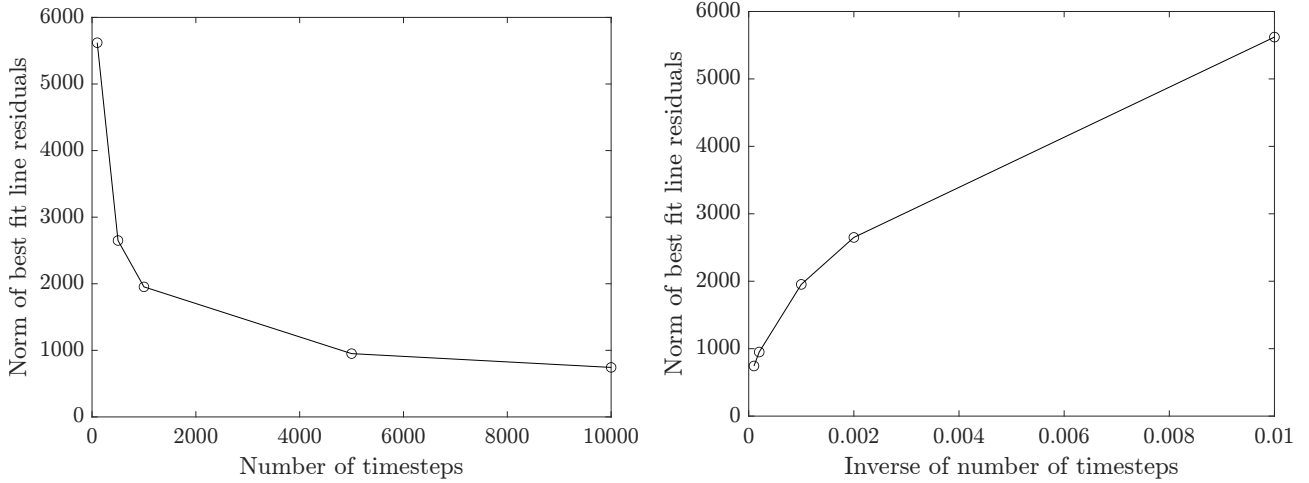


Figure 16: Best fit residuals vs number of time steps (left) and inverse of number of time steps (right).

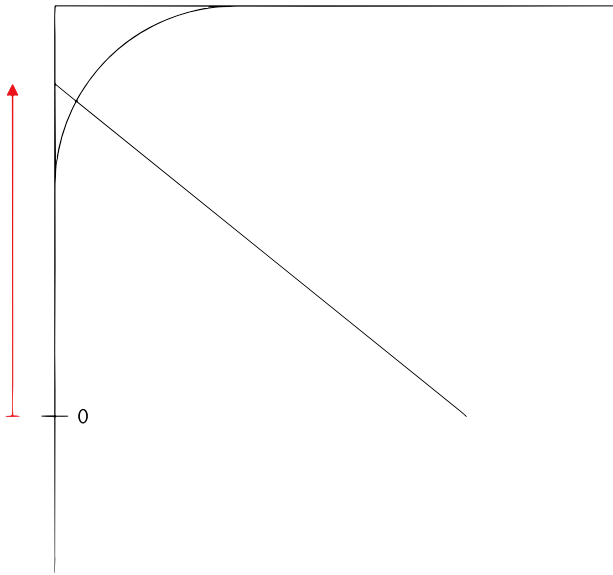


Figure 17: Equivalent square coordinate illustration.

3.5.4 Stagnation point Stanton number

Due to the significant statistical noise present near the stagnation point of the cube, an average over the five datapoints above and the five datapoints below the stagnation point was employed to calculate the Stanton number ratios.

3.6 Validation of results

To validate the results of the simulations, drag coefficient values were calculated for both the rounded square and sphere. Experimental evidence at Mach 5 was found for cubes at an unknown Knudsen number in pure continuum regime [45], and for spheres at a Knudsen number of 0.1 [46]. The drag coefficient values were thus computed at $Kn = 0.001$ for the square (lowest available Kn) and $Kn = 0.1$ for the sphere. It has to be pointed out that since mesh convergence was not proven for the square simulation with $Kn = 0.001$, its drag coefficient value might not be perfectly accurate. Given the low dependence of C_D values on the grid size observed in 3.4.1, this value was still considered representative

enough. As it is possible to see from Table 5, good agreement was found between the experimental and simulation values.

Table 5: Comparison of experimental and simulation drag coefficients for a cube and a sphere.

	Experiment	Simulation
Cube	1.67	1.7282
Sphere	1.63	1.6175

Stanton number values for a sphere were also compared. The sphere simulations showed a stagnation point Stanton number of around 0.7 for a Knudsen number of 1, while literature [47] showed an experimental value of around 0.8. These discrepancies could be caused by the choice of collision model or the diffusion accommodation coefficient. Data for the stagnation point Stanton number on a cube at comparable Knudsen numbers to those available from simulation was not found in literature.

Overall, given the good agreement between the drag coefficient values and the sphere Stanton number, the validation was considered successful and the simulations were judged sufficiently accurate.

4 Results and discussion

4.1 Variation of global Knudsen number results

Figure 18 shows the velocity contour around a rounded corner square for varying values of Knudsen number.

A radical change in flow conditions can be observed as the Knudsen number is increased. At a Kn of 0.001, in the pure continuum regime, a number of classical features of supersonic flow can be pointed out: an instantaneous bow shock in front of the cube, expansion fans at its corners and two shocks generated by the expanded flow impinging on itself aft of it. As the Knudsen increased to 0.01 and then to 0.05, a gradual thickening of the boundary layer, typical of a decrease in Reynolds number can be spotted. Moreover, the expansion fans and the shock at the back become gradually less noticeable, and the instantaneous bow shock at the front starts to gradually smear. By $Kn = 0.1$, the shock has become very smeared, and the boundary layer has thickened by a very significant amount. Between the Knudsen numbers of 0.5 and 5, a drastic flow change occurs: the shockwave completely disappears, replaced by a zone of reduced velocity occupying the entire front section of the domain. As Knudsen number is increased even further, this effect becomes more evident, and a peculiar triangular structure (the origin of which his unknown) appears in the wake of the cube.

This drastic change in flow behaviour could be explained with a paradigm shift in thought process: as mentioned many times, the flow based description of aerodynamics ceases to be valid at high Knudsen number, and it has to be replaced by a particle based one.

In the continuum regime, the flow impinging on the stagnation surface of the cube is forced to curve, first towards the corners and then around them. In a particle sense, when molecules that hit the surface of the cube are reflected in the opposite direction, they encounter other molecules that stop them from travelling against the flow and force them to curve. This produces a bow shock. However, as the Knudsen number is increased (and thus the density falls), the number of particles forward of those that have just reflected off the surface decreases. Thus, a greater distance is necessary for particles travelling in the opposite direction to be redirected. This can be seen from Figure 19.

At very high Knudsen numbers the "stopping effect" disappears almost entirely. Molecules that reflect off the stagnation surface are free to move in the opposite direction, effectively generating a second, completely separate flow.

The reduced velocity magnitude seen in front of the cube is thus probably an artefact, produced by the software as described in Equation 14 by averaging the velocity values of the particles belonging to the two flows over the cell area.

Figure 20 shows the distribution of heat transfer along the square contour for varying values of Knudsen number. A very significant reduction in heat transfer is observed with increased Knudsen number. This is probably caused by the decrease in density of the flow.

Figure 21 shows the heat transfer contours normalised by stagnation point heating. Peaks in heat transfer similar to those noted in [15] can be seen at the corners of the square for low Knudsen numbers. These peaks, however, disappear as the Knudsen number is increased. This is probably due to the change in flow physics explained above: as the flow is not forced to turn around the corner, its velocity does not increase and as a result the heat transfer profile flattens out.

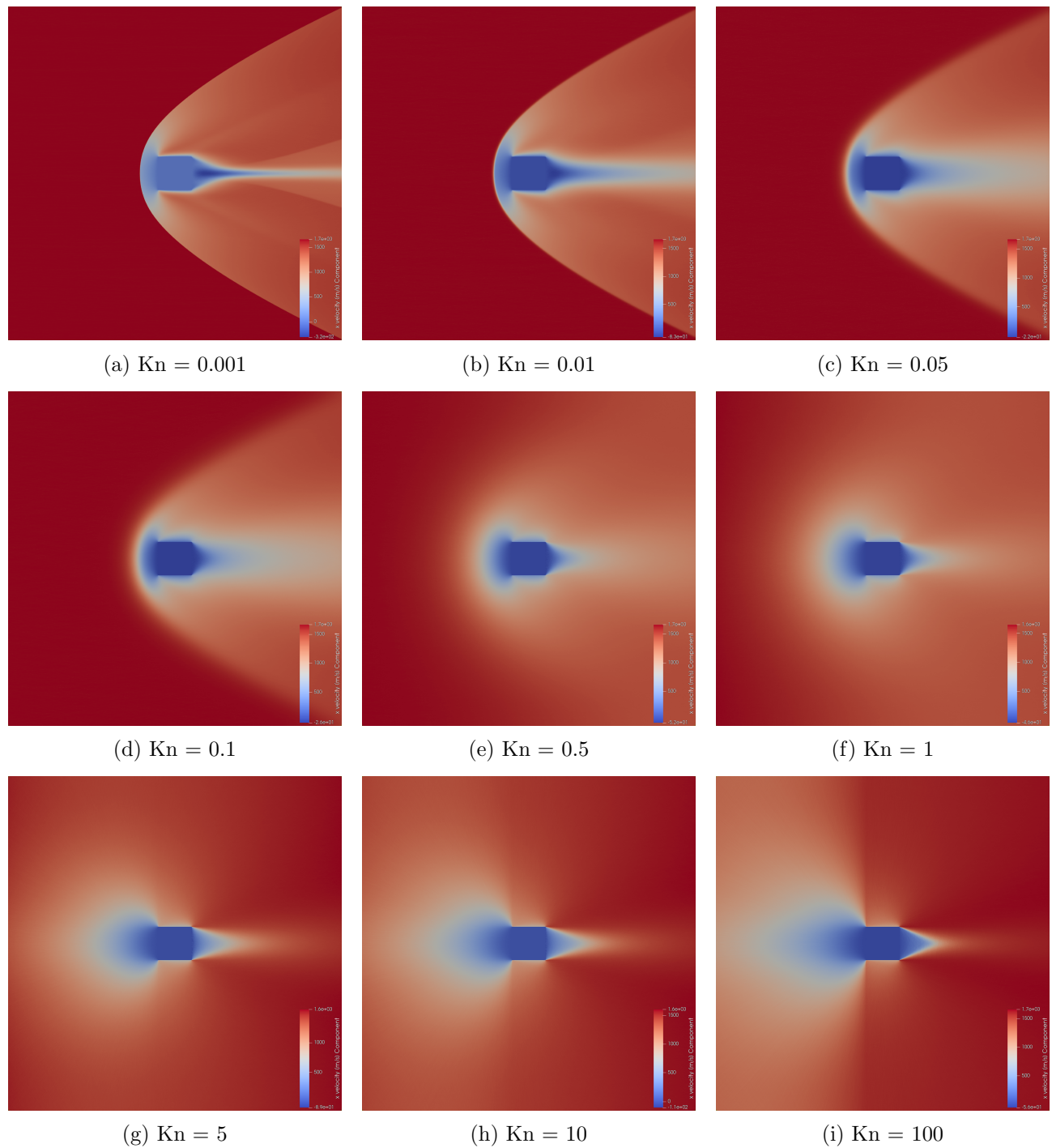


Figure 18: Velocity contours around a rounded square for varying Knudsen number.

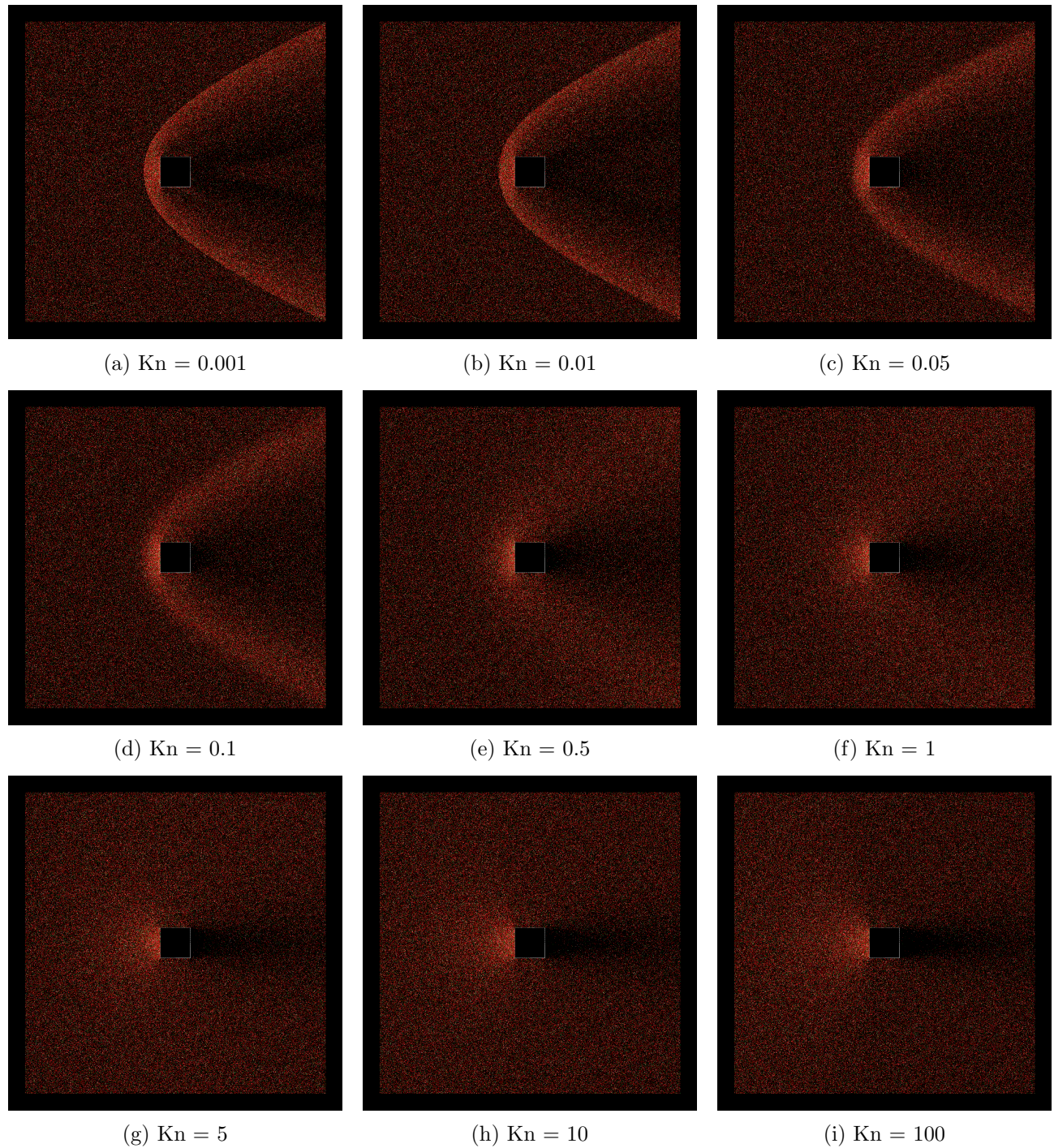


Figure 19: Particle contours around a rounded square for varying Knudsen number.

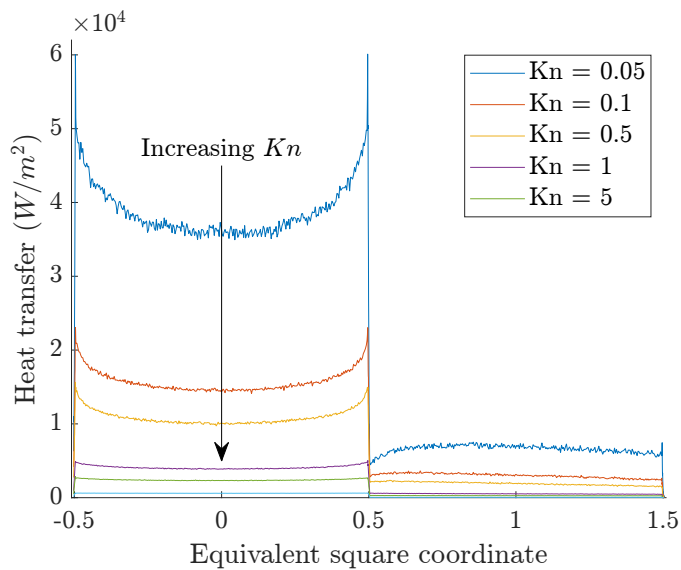


Figure 20: Distribution of heat transfer along the square contour for varying values of Knudsen number

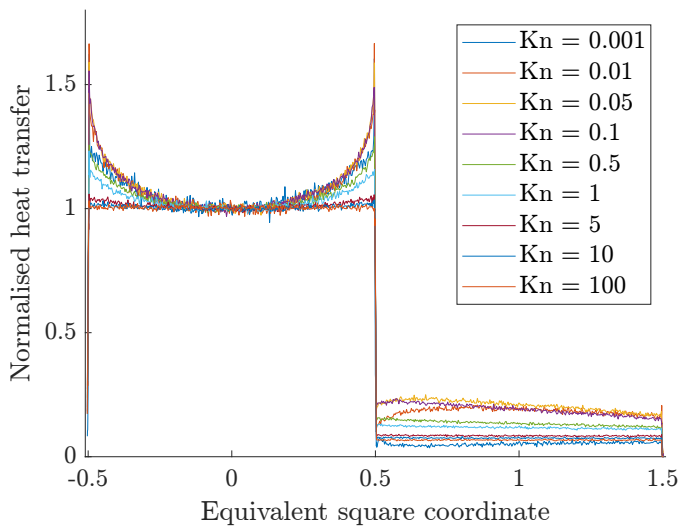


Figure 21: Distribution of normalised heat transfer along the square contour for varying values of Knudsen number

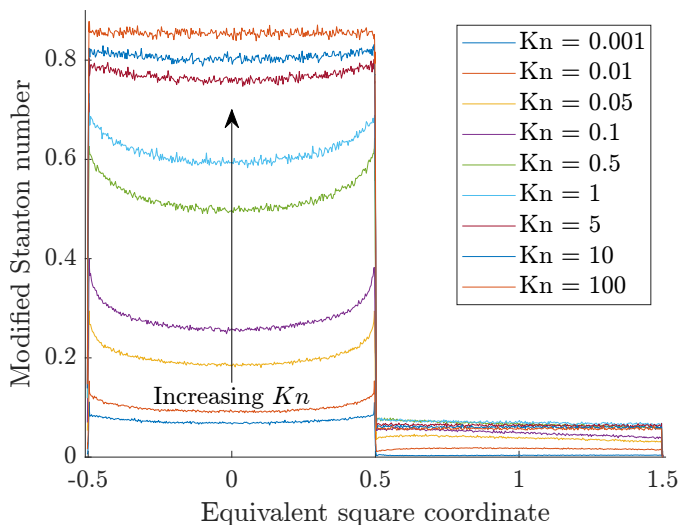


Figure 22: Distribution of modified Stanton number along the square contour for varying values of Knudsen number

Figure 22 shows the distribution of modified Stanton number along the square contour for varying of Knudsen numbers. The significant increase in Stanton number seen with increasing Knudsen number can again be probably explained by the change in flow physics with Knudsen number: as Kn is increased, the high density region between the shock and the cube's stagnation surface gradually dissipates, disappearing completely at very high Knudsen numbers. Consequently, the particles that collide with the cube's surface lose less energy, as they don't undergo collisions with molecules in the high-density region. This results in an higher energy transfer during the subsequent impact with the cube, leading to an increase in Stanton number.

Similar flow physics and heating trends were observed for a circle geometry. They can be seen in Figure 23 and Figure 24.

The variation in stagnation point Stanton number observed in Figure 22 and Figure 24 have been plotted respectively in Figure 25a and Figure 25b, with respect to the global Knudsen number, calculated based on the square side length. The observed pattern is partly matched by the one observed in literature for spheres [47], shown in Figure 26. The behaviour for Knudsen numbers below 0.01 could not be compared, due to lack of experimental data.

The variation in ratio between the peak and stagnation point Stanton number has been calculated and plotted against the local Knudsen number at the square corner. It can be seen in Figure 27. The trend shown by it mostly appears as it would have been expected based on the intuition gained from the velocity contours above. The point at $Kn = 0.1$ is however, shows a slightly lower value from the peak at $Kn = 1$. The reason for this dip is not entirely clear, and will be discussed more in depth in subsection 4.5.

4.2 Variation of edge radius results

Figure 28 shows the distribution of heat transfer around the geometry for varying values of edge radius. Note that, for clarity reasons, not all of the simulation cases have been included. It is possible to note that as the corner radius is increased, the reduction in heat transfer past the corner peak becomes more gradual, and the two peaks at the square edged coalesce into one. Because of the same effect, the heat transfer at the stagnation point gradually increases.

Comparing Figure 28 to Figure 20, reveals that the order of magnitude reduction in heat transfer has disappeared, as the global Knudsen number (and thus the density) has been kept constant.

Figure 29 shows the Stanton number distribution around the geometry for varying values of edge radius (again, for clarity reasons only the test cases with comparatively small edge radius have been included). The distributions follows closely the one included in Figure 22 for $Kn = 0.01$, and very little change is observed for the peak Stanton number values (corresponding to the 0.5 point on the equivalent square coordinate axis) for varying values of edge radius.

Plotting the Stanton number ratio against the local Knudsen number at the square corner (as shown in Figure 30) reveals an interesting trend. In the initial section of the Knudsen number range, the Stanton number ratio monotonically increases. However, as the local Knudsen number goes above 1, the Stanton ratio becomes virtually independent of it.

This effect can be explained as follows: in the first part of the Knudsen number range the coalescence effect explained above is significant: as the edge radius is decreased, and thus Knudsen number is

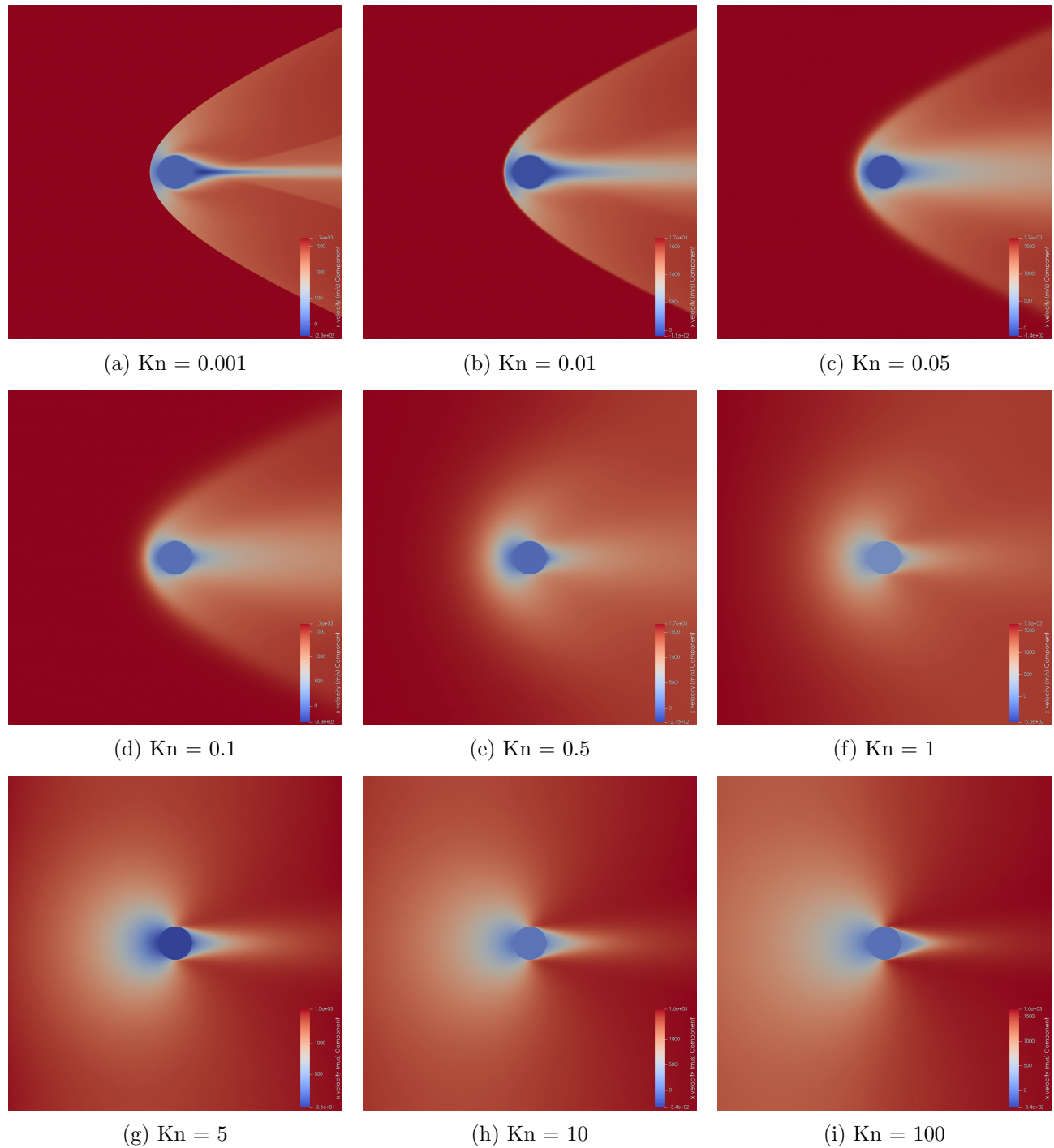


Figure 23: Velocity contours around a circle for varying Knudsen number.

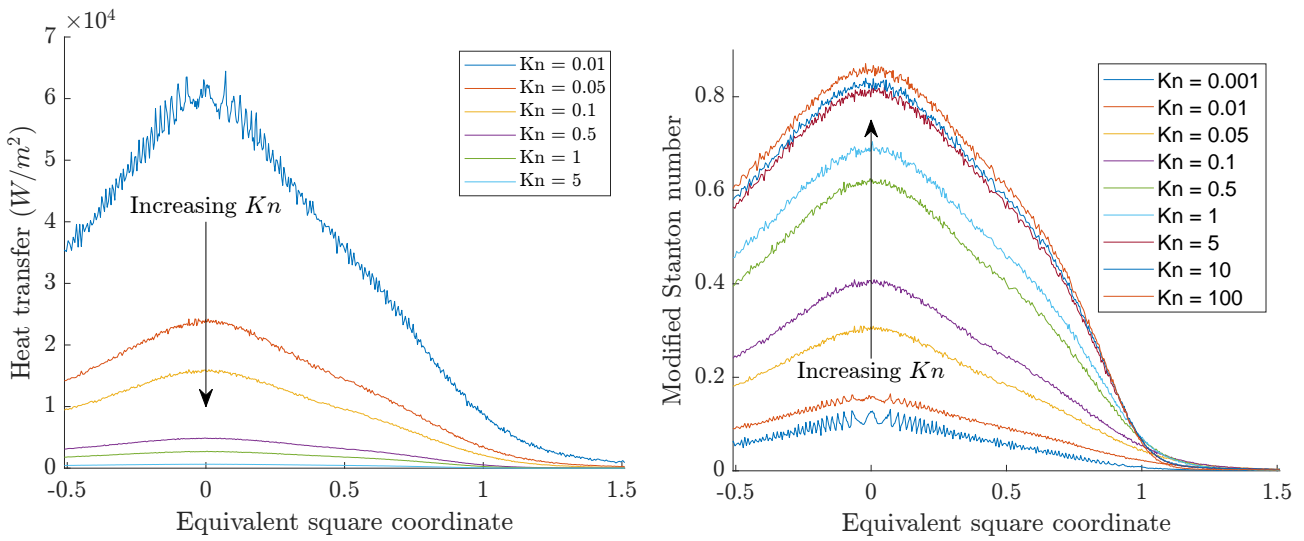


Figure 24: Heating (left) and stagnation Stanton number (right) distribution around a circle for varying Knudsen number.

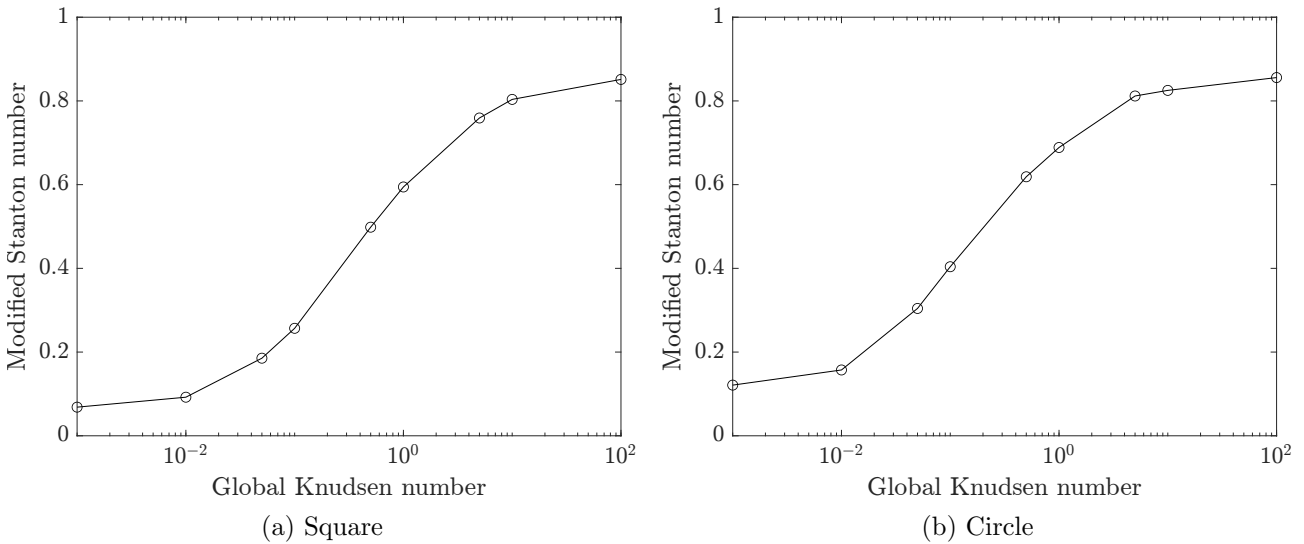


Figure 25: Stanton number vs global Knudsen number for a rounded square (a) and circle (b).

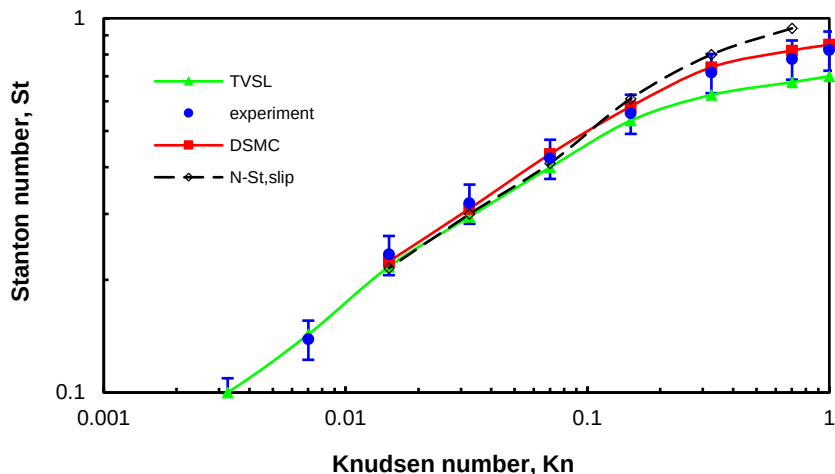


Figure 26: Stanton number vs global Knudsen number from literature [47].

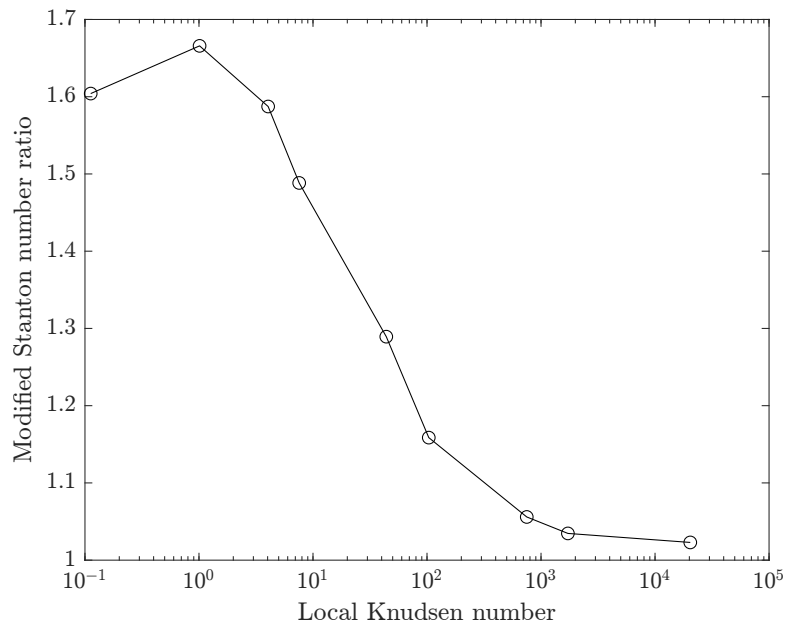


Figure 27: Stanton number ratio vs local Knudsen number for the varying global Knudsen number test case.

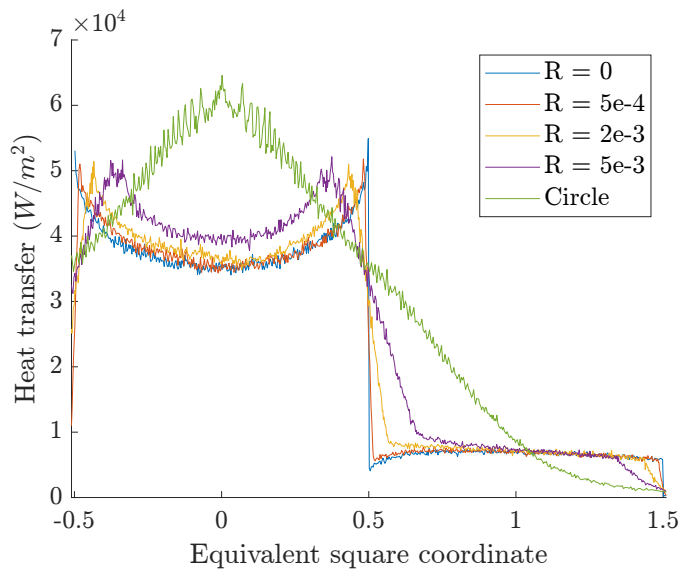


Figure 28: Distribution of heat transfer along the square contour for varying values edge radius.

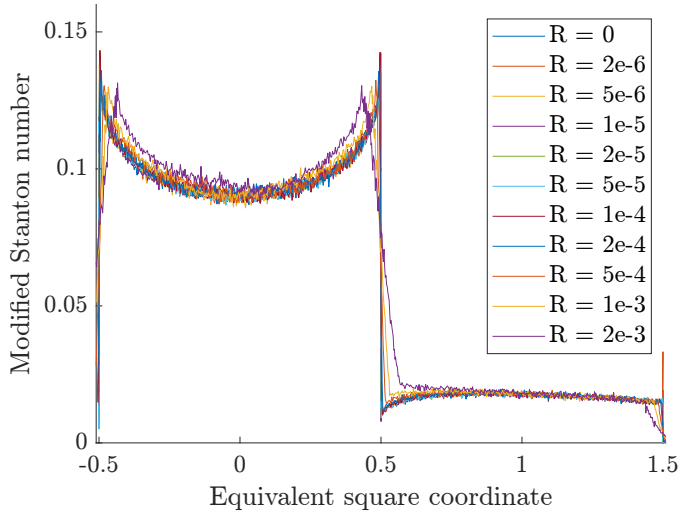


Figure 29: Distribution of Stanton number along the square contour for varying values edge radius.

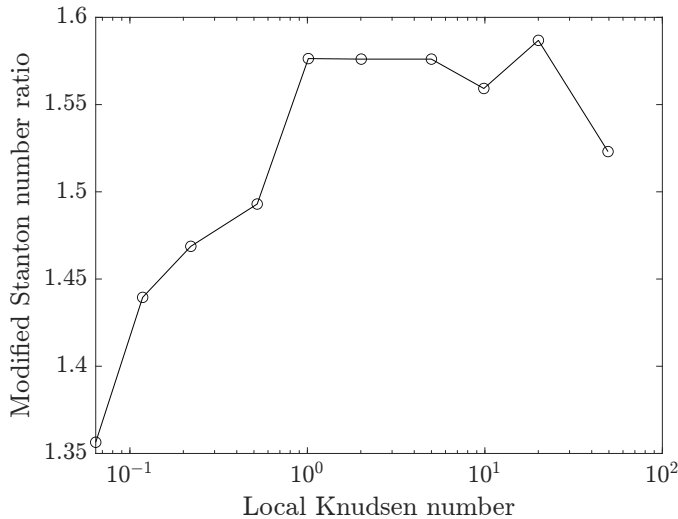


Figure 30: Stanton number ratio vs local Knudsen number for the varying edge radius test case. Note that the datapoints included are the ones from the test cases in Figure 29.

increased, the two peaks at the square corners are still separating, and the stagnation point heating is reducing. the ratio between the Stanton numbers at the two locations is thus increasing. Beyond a certain radius threshold, the geometry becomes virtually indistinguishable from a perfect square, and the effect stops being relevant.

The second section of the graph also gives some relevant insight: as the Stanton ratio does not increase or decrease with local Knudsen number, the change observed in Figure 27 could be only due to a change in global Knudsen number.

4.3 Constant local Knudsen number results

Figure 31 and Figure 32 respectively show the heat transfer and Stanton number distribution along the square contour for the constant local Knudsen number case. As shown in Table 3, a radius reduction corresponded to an equivalent Knudsen number increase, with the aim of maintaining the local Knudsen number constant. This objective was unfortunately not reached, as the theorised proportionality between local and global Knudsen numbers proved to not be valid.

Features noted when independently varying global Knudsen number and edge radius are both present, such as the more gentle decrease in heat transfer past the square corner or the order of magnitude increase in heat transfer. From Figure 32 it is possible to note the presence of a Stanton number peak at the corner of the $Kn = 10$ case. Computing the local Knudsen number (equal to approximately 2×10^5) reveals that this peak is probably caused by a very significant local rarefaction zone.

Figure 33 shows the variation in Stanton number with local Knudsen number for the constant local Knudsen number case. The trend looks very similar to the one observed in Figure 27.

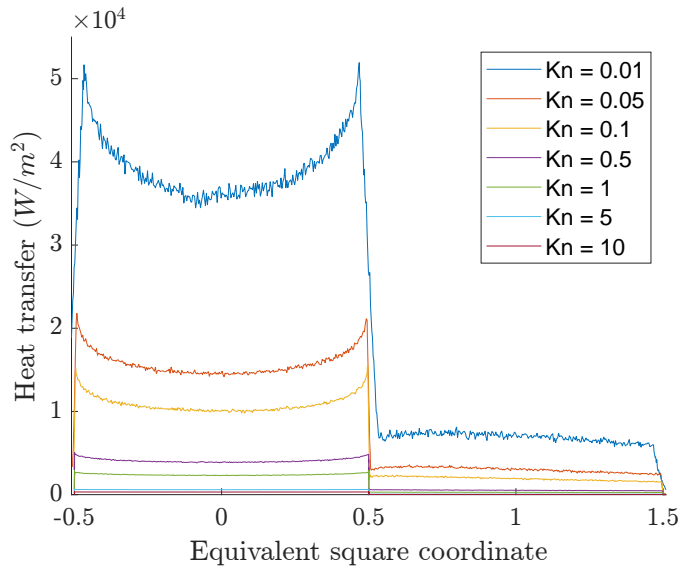


Figure 31: Distribution of heat transfer along the square contour for constant local Knudsen number case.

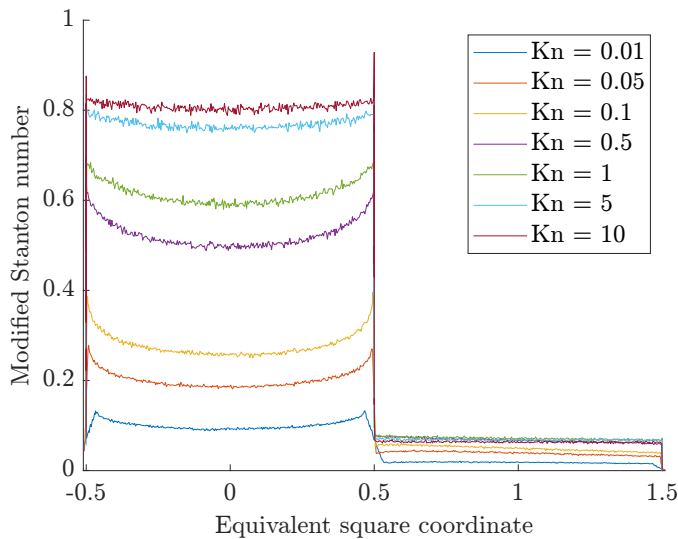


Figure 32: Distribution of Stanton number along the square contour for constant local Knudsen number case.

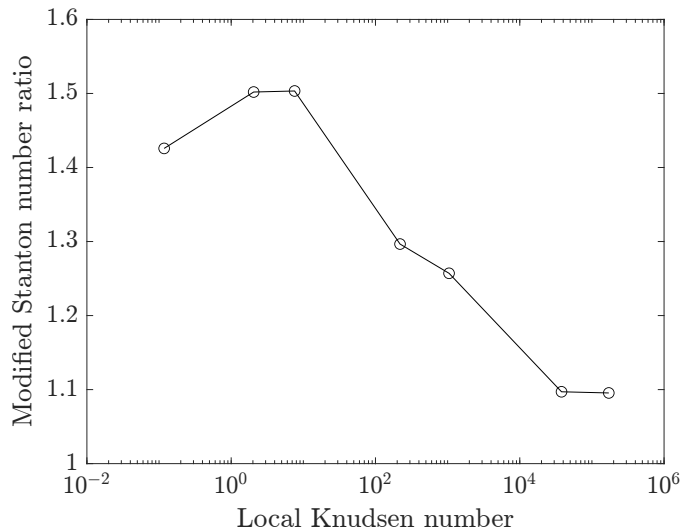


Figure 33: Stanton number ratio vs local Knudsen number for constant local Knudsen number case.

4.4 Variation of angle of attack results

Figure 34 shows the distribution of heat transfer along the square contour for varying values of angle of attack. As it is possible to see from it, the increase in heat transfer seen in literature [28, 29] has also been observed here.

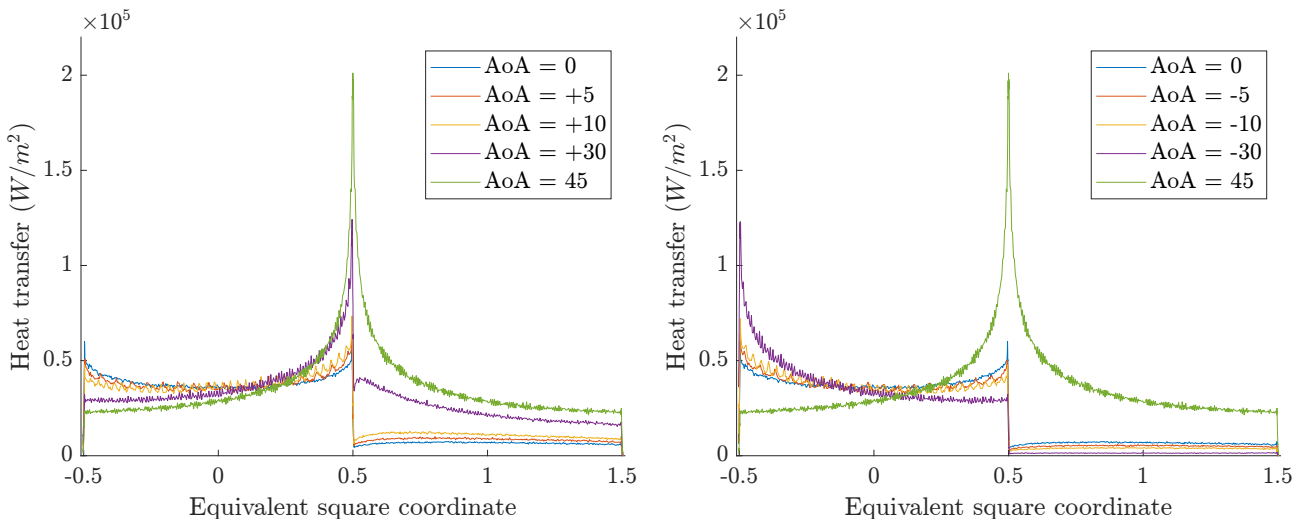


Figure 34: Distribution of heat transfer along the square contour for varying values of angle of attack.

4.5 Comparison of Stanton number ratio results

The results obtained for the Stanton number variation with Knudsen number from the three test cases appear to be almost contradictory. The varying Knudsen number simulations show an explicit dependence on Knudsen number. This, coupled with the results of the varying radius simulations, which show an explicit independence of Stanton number with corner radius, would lead to believe that the change in Stanton number is only due to a change in density. However, if this was the case, the constant local Knudsen number simulation would have to only be dependent on global Knudsen number, and thus replicate the section of Figure 27 between the $Kn = 1$ and $Kn = 100$ (as the global Knudsen numbers of these datapoints match the ones used for the constant local Knudsen number simulations).

The decrease in ratio observed in Figure 27 and Figure 33 is also of unknown origin. If it had been only observed in the varying Knudsen number case it could have probably been attributed to an unconverged mesh, as grid independence was not proven for a global Knudsen number of 0.001. However, the fact that this decrease has also been seen in the constant local Knudsen number case invalidates this theory, since the global Knudsen number for the first datapoint was equal to 0.01 (which was validated by mesh convergence)

Overall, this phenomenon appears to be quite complex, and further research is needed to identify a satisfactory correction factor to be implemented in rapid prototyping codes. This further research could be directed into modelling the lower Knudsen number regions through pure CFD or coupled DSMC-CFD codes, in order to provide some useful insight for the development of a valid correction factor.

4.6 General considerations on the Direct Simulation Monte Carlo technique

Direct Simulation Monte Carlo has overall proven to be a very useful and precise tool for the analysis of rarefied flows. Its computational cost prevents it however from leaving the academic setting, as powerful computing clusters are required for accurately simulating even very small domains: in the work carried out for this research thesis most of the simulations were run over multiple days on 40 state of the art server computing cores, despite the domain being limited to a 30 by 30 cm 2D square. Employing this tool for full 3D simulations, larger domains or the modelling of the pure continuum regime remains thus still unfeasible, if not through the use of coupled DSMC-CFD codes or very powerful supercomputers.

5 Conclusion and future work

The objective of this research was to analyse the effect of local and global rarefaction zones on the heat transfer onto simple shapes.

In section 1 a significant increase in the interest in space exploration was highlighted, and the need for new aerodynamic decelerators was evidenced. Moreover, it was pointed out that research into hypersonic rarefied flows is needed to develop the aforementioned aeroshells.

In section 2 the theoretical background for rarefied flow was outlined, and relevant research in the field examined. It was discovered that the optimal way to model this flow regime is through Direct Simulation Monte Carlo.

In section 3 the working principles of DSMC were outlined, and four set of simulations on simple shapes (varying global Knudsen number, varying edge radius, constant local Knudsen number and varying angle of attack) were designed based on them. Convergence studies were thus conducted and the simulation results were validated, in order to ensure the accuracy of the simulations.

In section 4 the main findings were presented:

- A drastic change in flow physics with rarefaction was noted, and a theoretical explanation was provided.
- The dependence of stagnation point Stanton number on global Knudsen number was evidenced and verified through comparison with literature.
- The dependence of the ratio between peak and stagnation point Stanton number with Knudsen number was investigated, in order to determine a correction factor for aerothermodynamic rapid prototyping codes. It was however discovered that further research is required, directed especially towards the continuum flow regime.

Overall, the research conducted can be considered successful regarding the investigation into the effects of rarefaction. More work is however needed to obtain a valid correction factor.

References

- [1] Paul Bruce. Aero70005 - aerothermodynamics of launchers and re-entry vehicles lecture notes, Oct 2023.
- [2] Ethiraj Venkatapathy, Kenneth Hamm, Ian Fernandez, James Arnold, David Kinney, Bernard Laub, Alberto Makino, Mary McGuire, Keith Peterson, Dinesh Prabhu, David Empey, Ian Dupzyk, Loc Huynh, Prabhat Hajela, Peter Gage, Austin Howard, and Dana Andrews. Adaptive deployable entry and placement technology (adept): A feasibility study for human missions to mars. *21st AIAA Aerodynamic Decelerator Systems Technology Conference and Seminar*, 2011. doi: 10.2514/6.2011-2608.
- [3] Brandon Smith, Bryan Yount, Carl Kruger, Chad Brivkalns, Alberto Makino, Alan Cassell, Kerry Zarchi, Ryan McDaniel, James Ross, Paul Wercinski, Ethiraj Venkatapathy, Gregory Swanson, and Nili Gold. Nano-adept aeroloads wind tunnel test. pages 1–20. IEEE, Mar 01, 2016. doi: 10.1109/AERO.2016.7500719.
- [4] E. Bassano, R. Savino, C. Richiello, G. Russo, R. Aurigemma, and F. Punzo. Irene - italian re-entry nacelle for microgravity experiments. 62nd International Astronautical Congress, Cape Town, SA, Jan 01, 2011. International Astronautical Federation. doi: 10.13140/2.1.3811.2642. URL https://explore.openaire.eu/search/publication?articleId==datacite____::1f3b3ef287b959dc8444afb54eebf3da.
- [5] David Jurewicz, Leo Lichodziejewski, Ben Tutt, Brian Gilles, and Glen Brown. Application of inflatable aeroshell structures for entry descent and landing. pages 1–10. IEEE, 2013. ISBN 1095-323X. doi: 10.1109/AERO.2013.6497412. ID: *cdi_ieee_primary_6497412*.
- [6] Christopher Cerimele, Edward Robertson, David Kinney, John Theisinger, Ronald Sostaric, Charles Campbell, Phil Robinson, Daniel Matz, Breanna Johnson, Susan Stachowiak, Joseph Garcia, and Jeffrey Bowles. A rigid mid-lift-to-drag ratio approach to human mars entry, descent, and landing. Hampton, Jan 09, 2017. NASA/Langley Research Center.
- [7] Danielle O'Driscoll, Paul J. K. Bruce, and Matthew Santer. Design and dynamic analysis of rigid foldable aeroshells for atmospheric entry. *Journal of spacecraft and rockets*, 58(3):741–753, May 2021. doi: 10.2514/1.A34845.
- [8] Michela Gramola, Paul J. Bruce, and Matthew J. Santer. Hypersonic foldable aeroshell for thermal protection using origami (hathor): aerothermal analysis. *AIAA SCITECH 2022 Forum*, Jan 2022. doi: 10.2514/6.2022-2288.
- [9] Danielle O'Driscoll, Michela Gramola, Tianshu Wang, Paul J. Bruce, and Matthew J. Santer. Design, construction, and mechanical testing of a rigid-deployable aeroshell for atmospheric entry. *AIAA SCITECH 2022 Forum*, Jan 1, 2019. doi: 10.2514/6.2022-1621.
- [10] Michela Gramola, Paul J. Bruce, and Matthew J. Santer. Engineering model for heat transfer to a complex-geometry deployable heat shield. *AIAA Scitech 2021 Forum*, 2021. doi: 10.2514/6.2021-0355.
- [11] Pietro Innocenzi, Michela Gramola, Tom B. Fisher, Mark K. Quinn, Paul J. K. Bruce, and Salvador Navarro-Martinez. Aerothermodynamic analysis of faceted aeroshell at hypersonic speed. In *HiSST: 2nd International Conference on High-Speed Vehicle Science Technology*, Sep 11, 2015 .
- [12] Paul A. Chambre. *Flow of Rarefied Gases*. Princeton University Press, 2017. ISBN 1400885809. doi: 10.1515/9781400885800. ID: alma991000661627801591.
- [13] Jian-Jun Shu, Ji Bin Melvin Teo, and Weng Kong Chan. Fluid velocity slip and temperature jump at a solid surface. *Applied mechanics reviews*, 69(2), Mar 1, 2017. doi: 10.1115/1.4036191.
- [14] Amit Agrawal, Hari Mohan Kushwaha, and Ravi Sudam Jadhav. *Burnett Equations: Derivation and Analysis*, pages 125–188. Springer International Publishing, Cham, 2020. ISBN 978-3-030-10662-1. doi: 10.1007/978-3-030-10662-1_5. URL https://doi.org/10.1007/978-3-030-10662-1_5.

- [15] Thomas W. Rees, Paul J. K. Bruce, Tom B. Fisher, Mark K. Quinn, and Jim A. Merrifield. Numerical and experimental studies of the hypersonic flow around a cube at incidence. *Acta astronautica*, 183:75–88, Jun 2021. doi: 10.1016/j.actaastro.2021.02.033. URL <https://dx.doi.org/10.1016/j.actaastro.2021.02.033>.
- [16] M. S Ivanov and S. F Gimelshein. Computational hypersonic rarefied flows. *Annual review of fluid mechanics*, 30(1):469–505, 1998. ISSN 0066-4189.
- [17] Maria Grazia De Giorgi, Donato Fontanarosa, and Antonio Ficarella. Modeling viscous effects on boundary layer of rarefied gas flows inside micronozzles in the slip regime condition. *Energy Procedia*, 148:838–845, 2018. ISSN 1876-6102. doi: <https://doi.org/10.1016/j.egypro.2018.08.113>. URL <https://www.sciencedirect.com/science/article/pii/S1876610218304077>. ATI 2018 - 73rd Conference of the Italian Thermal Machines Engineering Association.
- [18] Nam T.P. Le, Ahmad Shoja-Sani, and Ehsan Roohi. Rarefied gas flow simulations of naca 0012 airfoil and sharp 25-55-deg biconic subject to high order nonequilibrium boundary conditions in cfd. *Aerospace Science and Technology*, 41:274–288, 2015. ISSN 1270-9638. doi: <https://doi.org/10.1016/j.ast.2014.12.019>. URL <https://www.sciencedirect.com/science/article/pii/S1270963814002727>.
- [19] Apurva Bhagat, Harshal Gijare, and Nishanth Dongari. Modeling of knudsen layer effects in the micro-scale backward-facing step in the slip flow regime. *Micromachines*, 10(2), 2019. ISSN 2072-666X. doi: 10.3390/mi10020118. URL <https://www.mdpi.com/2072-666X/10/2/118>.
- [20] Apurva Bhagat, Harshal Gijare, and Nishanth Dongari. Implementation of knudsen layer phenomena in rarefied high-speed gas flows. *Journal of aerospace engineering*, 32(6), 2019. ISSN 0893-1321.
- [21] Guangming Guo and Qin Luo. Flowfield structure characteristics of the hypersonic flow over a cavity: From the continuum to the transition flow regimes. *Acta Astronautica*, 161:87–100, 2019. ISSN 0094-5765. doi: <https://doi.org/10.1016/j.actaastro.2019.05.023>. URL <https://www.sciencedirect.com/science/article/pii/S0094576519306356>.
- [22] D. Nabapure, A. Singh, and R.C.M. Kalluri. Investigation of rarefied flow over an open cavity using direct simulation monte carlo. *The Aeronautical Journal*, 127(1312):1009–1036, 2023. doi: 10.1017/aer.2022.89.
- [23] Xuhong Jin, Bing Wang, Xiaoli Cheng, Qiang Wang, and Fei Huang. Effects of corner rounding on aerothermodynamic properties in rarefied hypersonic flows over an open cavity. *Aerospace Science and Technology*, 110:106498, 2021. ISSN 1270-9638. doi: <https://doi.org/10.1016/j.ast.2021.106498>. URL <https://www.sciencedirect.com/science/article/pii/S1270963821000109>.
- [24] Deepak Nabapure and Ram Chandra Murthy K. Dsmc simulation of rarefied gas flow over a 2d backward-facing step in the transitional flow regime: Effect of mach number and wall temperature. *Proceedings of the Institution of Mechanical Engineers, Part G: Journal of Aerospace Engineering*, 235(7):825–856, 2021. doi: 10.1177/0954410020959872. URL <https://doi.org/10.1177/0954410020959872>.
- [25] Deepak Nabapure, Arjun Singh, and K. Ram Chandra Murthy. Effect of mach number on the rarefied gas flow over a forward-facing step. In Muthukumar Palanisamy, Velraj Ramalingam, and Murugan Sivalingam, editors, *Theoretical, Computational, and Experimental Solutions to Thermo-Fluid Systems*, pages 451–459, Singapore, 2021. Springer Singapore. ISBN 978-981-33-4165-4.
- [26] Deepak Nabapure and K. Ram Chandra Murthy. DSMC simulation of rarefied gas flow over a forward-facing step: Effect of expansion ratio. *AIP Conference Proceedings*, 2316(1), 02 2021. ISSN 0094-243X. doi: 10.1063/5.0036427. URL <https://doi.org/10.1063/5.0036427>. 030032.
- [27] Deepak Nabapure and Ram Chandra Murthy K. Dsmc investigation of rarefied gas flow over a 2d forward-facing step: Effect of knudsen number. *Acta Astronautica*, 178:89–109, 2021. ISSN 0094-5765.

- doi: <https://doi.org/10.1016/j.actaastro.2020.08.030>. URL <https://www.sciencedirect.com/science/article/pii/S0094576520305270>.
- [28] Rodrigo C. Palharini, Craig White, Thomas J. Scanlon, Richard E. Brown, Matthew K. Borg, and Jason M. Reese. Benchmark numerical simulations of rarefied non-reacting gas flows using an open-source dsmc code. *Computers & Fluids*, 120:140–157, 2015. ISSN 0045-7930. doi: <https://doi.org/10.1016/j.compfluid.2015.07.021>. URL <https://www.sciencedirect.com/science/article/pii/S0045793015002558>.
- [29] A. G. Klothakis, I. K. Nikolos, T. P. Koehler, M. A. Gallis, and S. J. Plimpton. Validation simulations of the DSMC code SPARTA. *AIP Conference Proceedings*, 1786(1), 11 2016. ISSN 0094-243X. doi: 10.1063/1.4967566. URL <https://doi.org/10.1063/1.4967566>. 050016.
- [30] G. Malaikannan, R. Kumar, and A.K. Chinnappan. A novel efficient hybrid dsmc-dynamic collision limiter algorithm for multiscale transitional flows. *International Journal for Numerical Methods in Fluids*, 86(9): 565 – 81, 2018/03/30. ISSN 0271-2091. URL <http://dx.doi.org/10.1002/fld.4466>. novel efficient hybrid DSMC-dynamic collision limiter algorithm;multiscale transitional flows;Direct Simulation Monte Carlo method;hybrid DSMC-DCL solver;DCL method;near-equilibrium flow regions;continuum breakdown parameter;nonequilibrium flow regions;2D parallel multispecies polyatomic particle-based hybrid flow solver;Dynamic Collision Limiter approach;nonequilibrium multiscale flows;K-S parameter;Kolmogorov-Smirnov statistical test;hypersonic flow;blunt body;aerospike;supersonic flow;rarefied flow;;
- [31] Zhonghua Li, Leining Dang, Yanguang Yang, and Zhihui Li. Study of hybrid NS-DSMC simulation method with chemical non-equilibrium for transitional hypersonic flow. *AIP Conference Proceedings*, 2027(1), 11 2018. ISSN 0094-243X. doi: 10.1063/1.5065269. URL <https://doi.org/10.1063/1.5065269>. 030175.
- [32] G. A. Bird. *The DSMC method*. [publisher not identified], Place of publication not identified, version 1.2. edition, 2013. ISBN 9781492112907.
- [33] Francis J. Alexander and Alejandro L. Garcia. The Direct Simulation Monte Carlo Method. *Computer in Physics*, 11(6):588–593, 11 1997. ISSN 0894-1866. doi: 10.1063/1.168619. URL <https://doi.org/10.1063/1.168619>.
- [34] Alejandro L. Garcia. Direct simulation monte carlo: Theory, methods, and open challenges. 2011.
- [35] Alexey Volkov. Me 491/591 non-equilibrium gas dynamics lecture notes, Jan 11, 2017.
- [36] Sparta users manual, -04-13 2023.
- [37] Andrew Brian Weaver. Assessment of high-fidelity collision models in the direct simulation monte carlo method, 2015. URL https://docs.lib.psu.edu/open_access_dissertations/586.
- [38] Aaron Pikus. Dsmc/sparta lecture 1 by aaron pikus, purdue university, Mar, 22 2019.
- [39] R. Maltsev. On the selection of the number of model particles in dsmc computations. *27th International Symposium on Rarefied Gas Dynamics 2010. Pts. 1 & 2*, 1333(1), Jan 1, 2011. doi: 10.1063/1.3562663. URL <https://search.proquest.com/docview/1448713170>.
- [40] Zhi-Xin Sun, Zhen Tang, Ya-Ling He, and Wen-Quan Tao. Proper cell dimension and number of particles per cell for dsmc. *Computers & fluids*, 50(1):1–9, Nov 1, 2011. doi: 10.1016/j.compfluid.2011.04.013. URL <https://dx.doi.org/10.1016/j.compfluid.2011.04.013>.
- [41] H. G. Weller, G. Tabor, H. Jasak, and C. Fureby. A tensorial approach to computational continuum mechanics using object-oriented techniques. *Computers in physics*, 12(6):620, Nov 1, 1998. doi: 10.1063/1.168744.
- [42] C. White, M. K. Borg, T. J. Scanlon, S. M. Longshaw, B. John, D. R. Emerson, and J. M. Reese. dsmcfoam+: An openfoam based direct simulation monte carlo solver. *Computer physics communications*,

- 224:22–43, Mar 1, 2018. doi: 10.1016/j.cpc.2017.09.030. URL <https://dx.doi.org/10.1016/j.cpc.2017.09.030>.
- [43] S. J. Plimpton, S. G. Moore, A. Borner, A. K. Stagg, T. P. Koehler, J. R. Torczynski, and M. A. Gallis. Direct simulation monte carlo on petaflop supercomputers and beyond. *Physics of fluids (1994)*, 31(8):86101, Aug 2019. doi: 10.1063/1.5108534. URL <http://dx.doi.org/10.1063/1.5108534>.
- [44] Iain D. Boyd. Direct simulation monte carlo for atmospheric entry. 1. theoretical basis and physical models. Technical report, Sep 2009. URL <https://apps.dtic.mil/sti/citations/ADA568174>.
- [45] Sergei I Gerasimov, Vladimir I Erofeev, Vasily A Kikeev, Vadim A Kuzmin, Alexei N Zharov, and Ilya A Novikov. Experimental and computational research of supersonic and hypersonic flow around cube shaped fragments in the air. *IOP Conference Series: Materials Science and Engineering*, 896(1):012127, jul 2020. doi: 10.1088/1757-899X/896/1/012127. URL <https://dx.doi.org/10.1088/1757-899X/896/1/012127>.
- [46] Eric Loth, John Tyler Daspit, Michael Jeong, Takayuki Nagata, and Taku Nonomura. Supersonic and hypersonic drag coefficients for a sphere. *AIAA Journal*, 59(8):3261–3274, 2021. doi: 10.2514/1.J060153. URL <https://doi.org/10.2514/1.J060153>.
- [47] Vladimir V. Riabov. *Numerical and Experimental Simulation Techniques in Hypersonic Low-Density Aerothermodynamics*. doi: 10.2514/6.2020-2416. URL <https://arc.aiaa.org/doi/abs/10.2514/6.2020-2416>.